



**Politecnico
di Torino**

Politecnico di Torino

MSc in Biomedical Engineering

Evaluating Hyponatremia Through Inferior Vena Cava Ultrasound: A Non-Invasive Approach to Volume Status Assessment

Candidate:

Sofia La Ferrera

Supervisors:

Prof. Luca Mesin
Ing. Piero Policastro

Academic Year 2024/25

Abstract

Hyponatremia, defined as serum sodium concentration of less than 135 mEq/L, is a common electrolyte disorder observed in hospitalized patients. Its diagnosis is clinically relevant due to the associated risk of increased morbidity and mortality. A critical step in managing hyponatremia is the correct assessment of the patient's volume status (hypovolemic, euvoletic, or hypervolemic), which guides therapeutic decisions. However, current diagnostic approaches, which are based on clinical evaluation, laboratory data, and static ultrasound assessments, often lack sensitivity and specificity, leading to frequent misclassifications. This thesis explores the integration of a novel software solution, developed by VIPER s.r.l, into current diagnostic methods for assessing volume status. The software enables semi-automated tracking of the inferior vena cava (IVC) walls in both transverse and longitudinal ultrasound views, to extract key parameters such as diameter, caval index (CI), respiratory caval index (RCI) and cardiac caval index (CCI). The primary objective was to develop and validate an accurate and reproducible automated classification model for volume status. The secondary aim was to identify a minimal subset of features capable of achieving reliable classification performance. The study enrolled 33 hyponatremic patients (21 females, 12 males; mean age 81.45 ± 12.78 years) who were classified as hypovolemic (6), euvoletic (14), or hypervolemic (13). Three machine learning classifiers were evaluated using 3-fold cross-validation. For all models, the inclusion of the full set of VIPER-derived features, in both short (SA) and long-axis (LA) views, significantly enhanced performance compared to using clinical variables alone. To identify the most predictive subset of features, a grid search was performed, restricted to all VIPER-derived features and two key clinical variables: edema and central venous pressure (CVP). During this feature selection phase, the Random Forest model consistently outperformed the other classifiers. As a result, the best-performing feature subset identified by Random Forest, comprising SA CCI, LA CCI, SA maximum diameter and edema, was selected for further evaluation. The final model, trained on this reduced feature set, was then evaluated with leave-one-out cross-validation (leaving out one patient per fold) to ensure an unbiased performance estimation. Concurrently, an intra-operator repeatability analysis of VIPER measurements was performed by calculating Intraclass Correlation Coefficients (ICC). The optimal Random Forest model, based on the reduced feature set, achieved a balanced accuracy of 82%. The repeatability analysis confirmed excellent consistency for measurements acquired in the short-axis view, with ICCs of 0.97 for diameter, 0.92 for RCI, and 0.90 for CCI. Measurements from the long-axis view demonstrated lower reproducibility (ICC 0.62-0.89). These findings suggest that integrating innovative VIPER features into machine learning models offers a non-invasive and reliable tool to support the differential diagnosis of volume status in hyponatremia. Future studies should focus on developing a fully automated classification system that relies exclusively on VIPER features.

Contents

List of Figures	4
List of Tables	7
1 Introduction	8
1.1 Principles of the Cardiovascular system	8
1.1.1 Pulmonary and Systemic Circuits	8
1.1.2 The Heart	9
1.1.3 Blood Vessels	11
1.1.4 Venous Function and Central Venous Pressure (CVP)	14
1.1.5 The Inferior Vena Cava (IVC)	15
1.1.6 Blood Volume Regulation and Perfusion	16
1.2 Principles of Respiratory System	17
1.2.1 Anatomy of the Respiratory System	18
1.2.2 Mechanics of Pulmonary Ventilation	19
1.2.3 Respiration effect on IVC	21
1.3 Principles of Renal Mechanisms of body fluid volume	23
1.3.1 Body fluid compartments	23
1.3.2 Renal regulation of extracellular fluid volume and osmolality	23
1.3.3 Disorders of Fluid Volume Regulation: Hyponatremia	25
1.3.4 Diagnostic approach to patients with Hyponatremia	26
2 Emerging Techniques for Indirect Assessment of Volume Status in Patients with Hyponatremia	29
2.0.1 Bioimpedance	29
2.0.2 Point-of-Care Ultrasound (PoCUS)	30
2.0.3 Inferior Vena Cava (IVC) Ultrasound	33
2.0.4 Summary and Clinical Relevance	34
3 Principles of Ultrasound	35
3.1 Ultrasound Probes and Imaging Modalities in Diagnostic Applications	39
3.2 US Imaging of the IVC	40
3.2.1 IVC Visualization: Longitudinal and Transverse Views	41
3.2.2 Imaging Modalities: B-Mode and M-Mode	41
3.2.3 IVC-Derived Indices	42

4	Material and Methods	43
4.1	Scanning Procedure and Equipment	43
4.2	VIPER	44
4.2.1	Pulsatility Indices Estimation	46
4.3	Dataset	48
4.3.1	Clinical and Ultrasound Data	48
4.4	Colab Environment and Python Frameworks	50
4.4.1	Analysis of Repeatability	50
4.4.2	Analysis of Group Differences and Feature Ranking for Group Discrimination	51
4.4.3	Analysis of ML models for classification	52
5	Results	55
5.1	Repeatability Analysis Results	55
5.2	Results of Group Comparison and Feature Ranking Analysis	58
5.3	Results of ML models analysis	64
6	Discussion of the Results	73
6.1	Statistical significances between groups	73
6.2	Interpretation of Machine Learning Model Performance	74
6.2.1	Added Value of VIPER Features	74
6.2.2	Evaluation of the feature selection	75
6.2.3	Selection of a Minimal and Interpretable Feature Subset	76
6.3	Repeatability of the measurements	77
6.4	Limits and Future Developments of the study	77
7	Conclusion	79

List of Figures

1.1	The blood flowing through the pulmonary and systemic circuits of the cardiovascular system.	9
1.2	Anatomical view of the heart illustrating atria, ventricles, atrioventricular valves, and major vessel connections.	10
1.3	Events of cardiac cycle for left ventricular function, showing changes in atrial, ventricular and aortic pressure.	11
1.4	Structural characteristics of the five blood vessel types.	14
1.5	Anatomy of the IVC and adjacent structures.	16
1.6	Anatomy of the respiratory system	19
1.7	The diagram shows the variations in lung volume, alveolar pressure, pleural pressure and transpulmonary pressure occurring during normal respiration.	21
1.8	Compliance diagram of the lungs.	21
1.9	Volume - pressure curve of a venous blood vessel, which shows the relationship between the vessel volume (V) and the transmural pressure (P _{tm}).	22
3.1	Illustration of Snell's Law.	37
3.2	Types of probe used in diagnostic	40
3.3	Longitudinal scan of IVC taken in two ultrasound modes. (a) B-mode allows to identify the IVC and the adjacent structures; (b) M-mode captures time-dependent changes in vessel diameter along a fixed direction.	42
4.1	Convex CA1-7AD transducer	44
4.2	Samsung HM70EVO ultrasound system	44
4.3	The graduated scale on the right indicates intervals of 10 mm per tick mark. The yellow rectangle highlights the sidebar, while the two red dots indicate a 5 cm segment used for the conversion factor.	45
4.4	Segmentation of the IVC edges in longitudinal view.	46
4.5	Segmentation of the IVC edges in transversal view.	46
4.6	IVC diameter over time and respiratory component (highlighted in bold) extracted by filtering.	47
4.7	IVC diameter over time and cardiac component (highlighted in bold) extracted by filtering.	48

5.1	Boxplot showing the distribution of intra-subject variance (over three acquisitions) across patients for SA collapsibility indices.	56
5.2	Boxplot showing the distribution of intra-subject variance (over three acquisitions) across patients for LA collapsibility indices.	57
5.3	Example frames from two long-axis acquisition videos for subject 22. In both videos the inferior vena cava (highlighted by the yellow rectangles) disappears partially or completely in some frames. This loss of visualisation forces the semi-automatic algorithm to segment a region that does not correspond to the actual vessel, leading to inconsistent measurement estimates and high intra-subject variability in the collapsibility indices.	58
5.4	Distribution of the clinical features from patients with different volemic condition (hypo-, eu-, hypervolemic). The plots visualize inter-group separation and within-group variability.	62
5.5	Distribution of VIPER-derived features across patients with different volemic conditions (hypo-, eu-, and hypervolemic). Group differences were evaluated using the Kruskal–Wallis test; H denotes the test statistic, and the associated p-value (from the chi-squared distribution) indicates the likelihood of observing such differences by chance. A p-value < 0.05 denotes statistically significant inter-group variation. The plots illustrate both inter-group separation and intra-group variability.	63
5.6	Bar plots showing the absolute frequencies of patients across volume status groups (hypo-, eu-, hypervolemic) for the binary features analyzed using Fisher’s exact test. Feature codings are as follows: Edema (0 = absent, 1 = present), CVP (0 = normal, 1 = elevated), and Sex (0 = female, 1 = male). The y-axis represents the number of patients in each category within the corresponding group.	64
5.7	Confusion matrices for different classifiers using only clinical and clinical +vipер variables.	66
5.8	Global ranking of weighted importance of the features selected by the Linear SVM model. The length of each bar is given by the product of the coefficient value and the selection frequency across folds. Bar colors indicate the sign of the coefficient: blue for positive and red for negative associations with the target variable. While the sign reflects the direction of the effect, the importance is determined by the absolute value of the coefficient, which reflects the strength of the contribution.	69
5.9	Global ranking of weighted importance of the features selected by the RF model. The bar length corresponds to the coefficient importance multiplied by the selection weight across folds.	69
5.10	Common features selected by both Linear SVM and Random forest classifiers.	70
5.11	PCA of the features selected by Linear SVC.	71

5.12 tSNE of the features selected by Linear SVC.	71
5.13 PCA of the features selected by Random Forest classifier.	71
5.14 tSNE of the features selected by Random Forest classifier.	71
5.15 PCA with the features selected by the grid search.	72
5.16 tSNE with the features selected by the grid search.	72

List of Tables

1.1	Approximate total cross-sectional area of different types of blood vessels in the systemic circulation.	12
4.1	Distribution of patients by target class	48
4.2	Clinical features included in the initial dataset.	49
4.3	Ultrasound features extracted using VIPER software.	50
5.1	Intraclass Correlation Coefficient (ICC) Results for Repeatability. . .	55
5.2	Mean Coefficient of Variation (CoV) for Intra-Operator Variability. .	55
5.3	Shapiro-Wilk normality test results for each variable across the three diagnostic classes.	59
5.4	Statistical test results for all features. Fisher’s exact test was used for categorical variables, and Kruskal-Wallis test for continuous ones. Statistically significant p-values ($p \leq 0.05$) are highlighted in bold. . .	60
5.5	Ranking of continuous features analyzed with the Kruskal-Wallis test, sorted by ascending p-value.	61
5.6	Performance of Logistic Regression classifier.	64
5.7	Performance of Linear SVC.	64
5.8	Performance of RF classifier.	65
5.9	Linear SVC selected features ordered by average importance. Both the coefficient importance and the mean selection weight across folds are reported.	67
5.10	RF selected features ordered by average importance. Both the coefficient importance and the mean selection weight across folds are reported.	68
5.11	Best-performing feature subset for Linear SVC selected via grid search. .	71
5.12	Best-performing feature subset for Random Forest selected via grid search.	72
5.13	Performance of the final model evaluated through leave-one-out cross-validation on the optimal subset of features.	72

Chapter 1

Introduction

This chapter provides an overview of the fundamental principles of the cardiovascular system, with particular emphasis on the functions of the heart, blood vessels, and the inferior vena cava (IVC), which is increasingly recognized as a valuable non-invasive marker for assessing volume status. It then proceeds to examine the respiratory system, focusing on the impact of ventilatory mechanics on IVC diameter variations. Finally, the chapter explores the renal mechanisms involved in body fluid regulation, providing a physiological foundation for understanding the pathophysiology and diagnostic classification of hyponatremia.

1.1 Principles of the Cardiovascular system

The cardiovascular system is a complex apparatus in charge of transporting blood, nutrients and waste products throughout the body. Its role is essential in supporting cellular function.

The cardiovascular system consists of:

- Heart
- Blood Vessels
- Blood

1.1.1 Pulmonary and Systemic Circuits

The circulatory system is divided into two interconnected but functionally distinct circuits (Figure 1.1):

- **Pulmonary Circuit** – The right side of the heart pumps deoxygenated blood to the lungs via the pulmonary arteries. In the pulmonary capillaries, gas exchange occurs: carbon dioxide diffuses out of the blood, and oxygen diffuses in. The now oxygenated blood flows back to the left atrium through the pulmonary veins.

- **Systemic Circuit** – The left side of the heart pumps oxygenated blood into the aorta, which distributes it to systemic organs and tissues. In systemic capillaries, oxygen and nutrients are delivered to cells, and carbon dioxide and metabolic waste products are collected. Deoxygenated blood returns to the right atrium via the superior and inferior venae cavae.

These two circuits operate in series, so blood must pass through both the pulmonary and systemic circuits in sequence. However, the blood flow within each circuit flows in parallel. This is because, at the same time, the right heart pumps blood to the lungs, while the left heart pumps blood to the system organs.

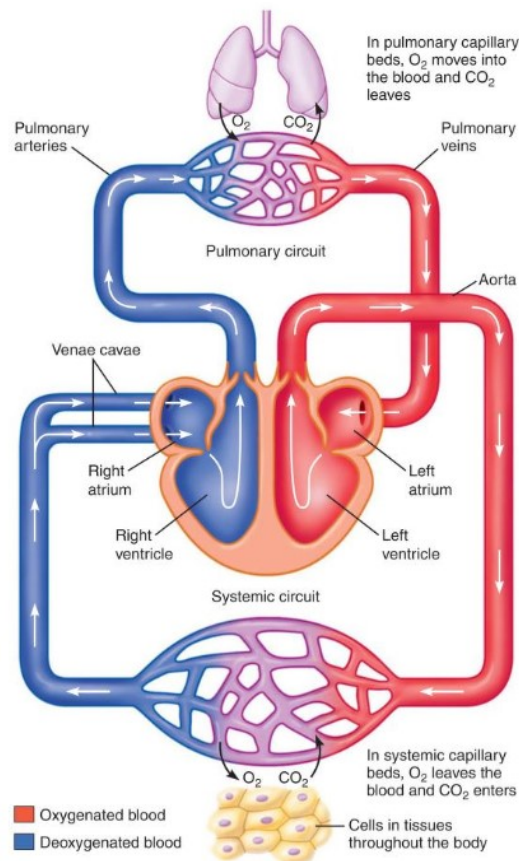


Figure 1.1: The blood flowing through the pulmonary and systemic circuits of the cardiovascular system.

1.1.2 The Heart

The heart is a muscular organ divided into two separate pumps: the right heart, which delivers deoxygenated blood to the lungs via the pulmonary circulation, and the left heart, which sends oxygenated blood to the systemic circulation. These two sides are separated by the interventricular septum, which prevents mixing of oxygenated and deoxygenated blood (Figure 1.2). Each side of the heart comprises two chambers:

- Atria (right and left), the upper chambers that receive blood returning to the heart via the venous system.
- Ventricles (right and left), the lower chambers that pump blood, received by atria, into the arterial system.

The atrioventricular (AV) valves, which are located between the atria and ventricles, ensure unidirectional blood flow. The tricuspid valve is situated between the right atrium and right ventricle, while the mitral valve is between the left atrium and left ventricle. Two more semilunar valves block the backflow from the arteries, which are the pulmonary valve (located between the right ventricle and the pulmonary artery) and the aortic valve (located between the left ventricle and the aorta).

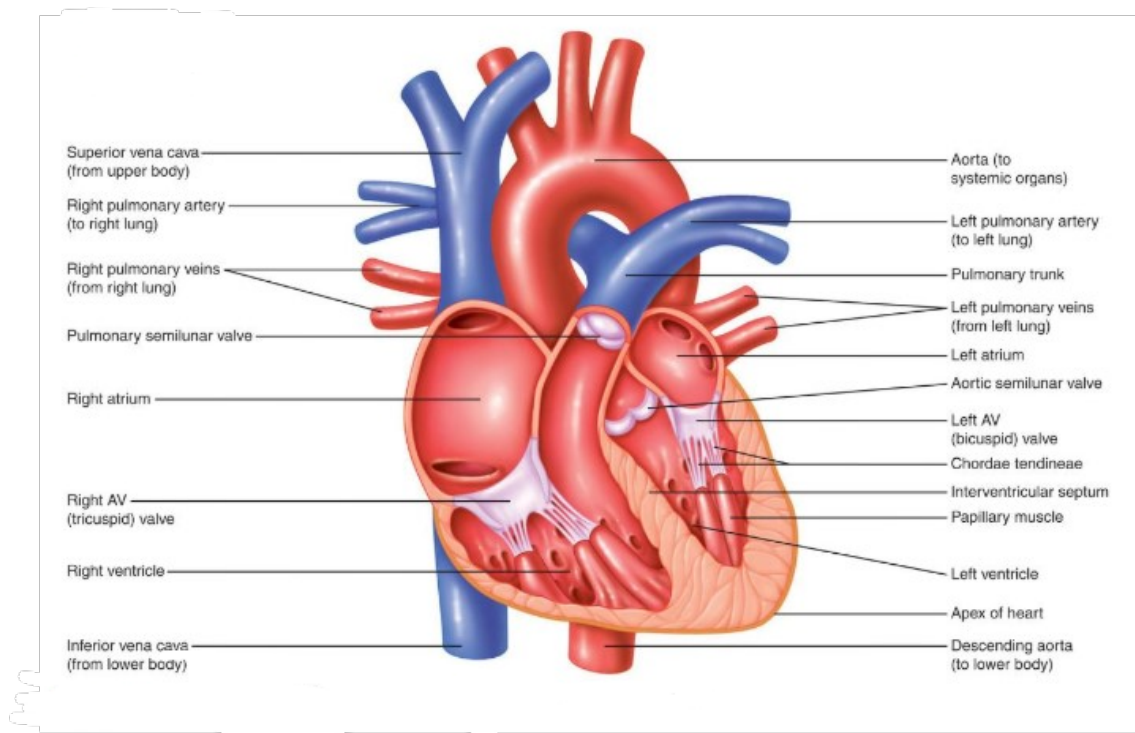


Figure 1.2: Anatomical view of the heart illustrating atria, ventricles, atrioventricular valves, and major vessel connections.

The heart operates through a sequence of contraction and relaxation known as the cardiac cycle (Figure 1.3), consisting of:

- Systole: the contraction phase, where ventricles eject blood
- Diastole: the relaxation phase, during which the heart fills with blood.

The cycle begins with atrial systole, pushing blood into the ventricles, so the ventricles contract with all valves closed. When intraventricular pressure exceeds arterial

pressure, semilunar valves open and blood is ejected. Following ejection, ventricular diastole begins with all valves closed, so there's no volume change. Then atrioventricular valves reopen as atrial pressure exceeds ventricular pressure. The sinus node, located in the right atrium near the superior vena cava, initiates each heartbeat. Its electrical impulse spreads through the atria and then, with a slight delay, reaches the ventricles via the atrioventricular bundle. This delay ensures the atria contract before the ventricles, enhancing ventricular filling [37].

Thus, the atria act as primer pumps, that increase the ventricular pumping effectiveness as much as 20 percent; and the ventricles serve as the main force for circulating blood through the pulmonary and systemic circuits.

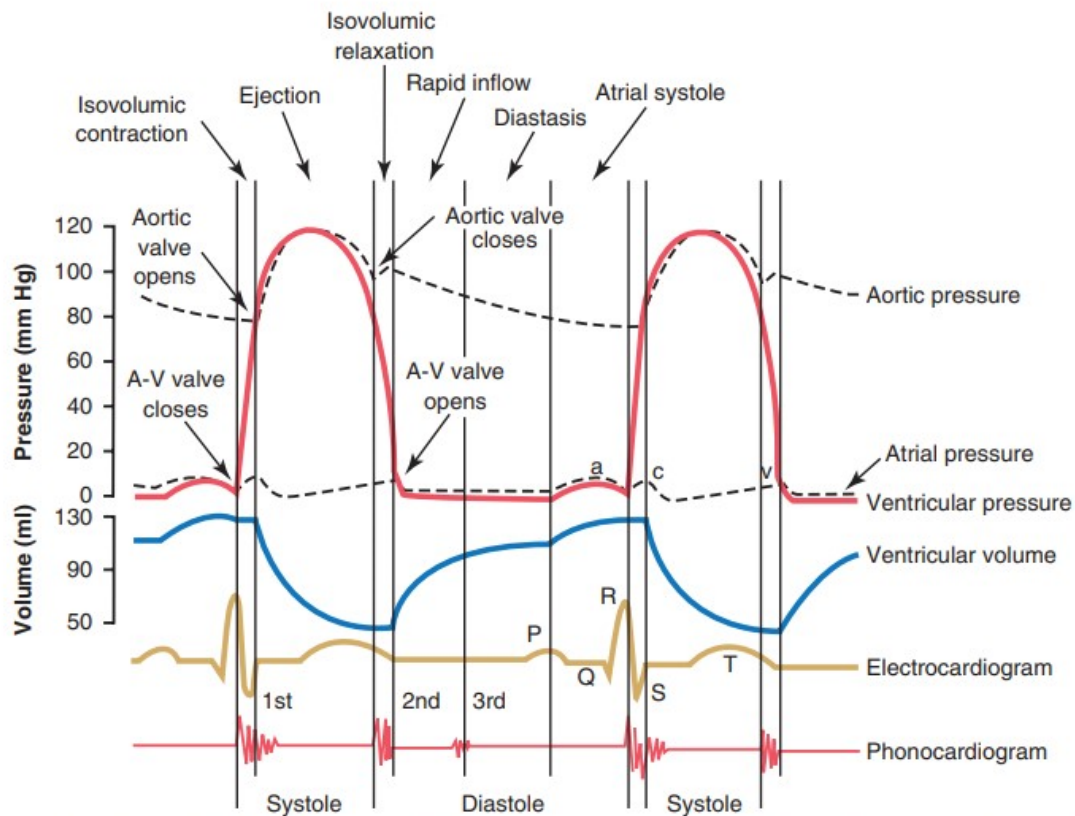


Figure 1.3: Events of cardiac cycle for left ventricular function, showing changes in atrial, ventricular and aortic pressure.

1.1.3 Blood Vessels

Blood vessels are classified anatomically and functionally into arteries, arterioles, capillaries, venules, and veins, each category playing a specific role in the transport, regulation, and exchange of blood and solutes. Approximately 84% of the total blood volume resides within the systemic circulation, with veins containing the majority (64%), followed by arteries (13%) and microcirculatory segments such as arterioles and capillaries (7%) [7]. A comparative analysis of the total cross-sectional area

of these vessels in the average adult highlights key physiological differences. As shown in Table 1.1, capillaries, despite their microscopic size, possess the highest total cross-sectional area (2500cm^2), facilitating efficient nutrient and gas exchange. In contrast, large conduit arteries such as the aorta have a minimal cross-sectional area (2.5cm^2), optimized for the rapid transport of blood under high pressure. The venous system, particularly venules and small veins, exhibits a significantly larger cumulative cross-sectional area than the arterial system (e.g., 250cm^2 for venules versus 20cm^2 for small arteries) [7]. This morphological feature underpins the veins' role as a capacitance reservoir, allowing for the accommodation of variable blood volumes with minimal changes in pressure.

Vessel Type	Cross-Sectional Area (cm^2)
Aorta	2.5
Small arteries	20
Arterioles	40
Capillaries	2500
Venules	250
Small veins	80
Venae cavae	8

Table 1.1: Approximate total cross-sectional area of different types of blood vessels in the systemic circulation.

Arteries and Arterioles

Arteries transport blood under high pressure from the heart to the tissues. Their walls are thick, composed of elastic and fibrous tissues, which enable arteries to withstand the relatively high blood pressures present in these vessels. The aorta, the largest artery, has a diameter of approximately 12.5 mm and a wall thickness of about 2 mm, while medium-sized arteries possess internal diameters ranging from 2 mm to 6 mm. These vessels offer minimal resistance and function as rapid conduits for blood transport [37]. A key mechanical property of arteries is their low compliance—meaning that, a small change in volume causes a large change in pressure. This is a direct consequence of their elastic walls. The combination of stiffness and elasticity allows arteries to expand during systole and recoil during diastole, functioning as pressure reservoirs. This mechanism ensures a continuous and smooth flow of blood through the circulation, even when the heart is in its relaxation phase and not actively ejecting blood [37]. As arteries branch and become smaller, they form arterioles, which serve as the passageway for blood to enter the capillaries. The structure of the vessel wall changes: the proportion of elastic tissue in their walls decreases while the amount of smooth muscle increases. This smooth muscle can contract or relax, thereby modulating the diameter of arterioles. This makes them act as critical control points, where resistance to blood flow can be regulated. This dynamic control over lumen diameter enables the redistribution of blood flow according to tissue-specific metabolic demands [7, 37].

Capillaries

Capillaries are the smallest and thinnest blood vessels, with walls composed of a single layer of endothelial cells. They connect arterioles and venules and represent the primary site for the exchange of gases, nutrients, electrolytes, hormones, and waste products between blood and surrounding tissues. Their thin walls and the presence of small pores facilitate efficient diffusion and filtration processes, which are essential for cellular function. Despite their small size, capillaries are crucial: this is where the most vital interactions between the blood and body tissues occur. Interestingly, even though they contain only about 7% of the systemic blood volume, they have the largest total cross-sectional area, which significantly slows down blood flow, maximizing the time available for exchange [7, 37].

Venules and Veins

Venules take the blood from the capillaries, then gradually merge into larger veins and return blood to the heart. As shown in Figure 1.4, veins are characterized by thinner walls than arteries, which make them about eight times more distensible than the arteries. The venous system operates under low pressure and has high compliance, which means that it can accommodate significant changes in blood volume with minimal changes in pressure. Compliance and distensibility are sometimes used interchangeably, but there are different things. Distensibility is the fractional change in volume per unit pressure, while compliance is distensibility multiplied by the volume in the vessel. Therefore, a highly distensible vessel with small volume may have lower compliance than a less distensibility vessel but with larger volume. Systemic veins, including the IVC, are about 8 times more distensible than arteries and contain about 3 times more blood volume, which result in a compliance 24 times greater than that of their arterial counterparts [7].

Veins contain unidirectional valves which are used to prevent backflow and help venous return, especially from the lower limbs. Another role of the veins, beside transporting blood, is that they act as a blood reservoir: about 64% of the systemic blood volume is stored in the venous system, which can be used as needed.

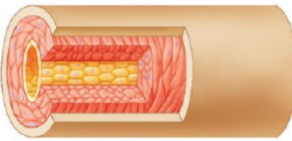

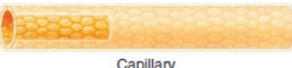

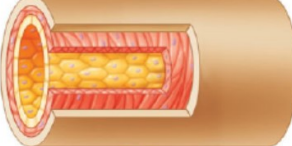
Average internal diameter (mm)	Average wall thickness (mm)		Special features
4.0	1.0	 Artery	Muscular, highly elastic
0.03	0.006	 Arteriole	Muscular, well innervated
0.008	0.0005	 Capillary	Thin-walled, highly permeable
0.02	0.001	 Venule	Thin-walled, some smooth muscle
5.0	0.5	 Vein	Thin-walled (compared to arteries), fairly muscular, highly distensible

Figure 1.4: Structural characteristics of the five blood vessel types.

1.1.4 Venous Function and Central Venous Pressure (CVP)

While the primary known function of the veins is returning deoxygenated blood to the heart, they also play several roles in the regulation of circulatory dynamics. One of their key roles is working as blood reservoirs: because of their ability to dilate and constrict, veins can store large volumes of blood and release it when needed. This helps maintain stable blood flow, especially in situations where the body needs to quickly adjust circulation. Another function is to push blood toward the heart, especially from the peripheral veins, by means of a venous pump. Through these mechanisms, veins help control venous return, which influences how much blood fills the heart before it contracts, and consequently regulate cardiac output. A key parameter to understand the function of the venous system is the Central Venous Pressure (CVP). CVP corresponds to the pressure in the right atrium, where all systemic veins drain. This pressure depends on two main factors: how well the right side of the heart pumps blood toward the lungs, and how much blood is returning from the peripheral circulation. If the right heart is pumping efficiently, it quickly pumps blood forward, resulting in a right atrial pressure decrease. Conversely, weakness of the heart lead to an increase of the right atrial pressure [7]. In clinical settings, CVP is often used as an indicator of a patient's volume status, especially in hospitalized or critically ill patients. A high CVP may suggest fluid overload, hypervolemia, or even right heart failure, while a low CVP might indicate hypovolemia or reduced venous return. However, CVP is not always a perfect measurement. Its values can

be influenced by several factors, including respiration, thoracic pressure, and patient positioning [31].

1.1.5 The Inferior Vena Cava (IVC)

The inferior vena cava (IVC), showed in Figure 1.5, is the largest vein in the human body, originates at the level of the fifth lumbar vertebra (L5), from the junction of the right and left common iliac veins. It ascends along the right side of the vertebral column, passes posterior to the liver, where it receives blood from the hepatic veins, and traverses the diaphragm to enter the right atrium of the heart. In healthy adults, the inferior vena cava (IVC) diameter ranges from 18 to 32 mm. In some cases, the term “mega cava” has been used to describe IVC up to 40 mm in diameter [36], which may indicate pathological conditions.

The IVC returns deoxygenated blood from the lower limbs, pelvis, and abdomen back to the heart. Its large internal diameter and thin wall make it suitable for transporting high volumes of blood under low pressure. One of the characteristics of the IVC is its high compliance, which means that it can accommodate significant changes in blood volume with minimal variation in pressure. This property is essential for its function as a dynamic blood reservoir and for adapting to physiological changes such as those occurring during respiration and the cardiac cycle. [39].

Vascular compliance is defined as the ratio of the change in volume (ΔV) to the change in transmural pressure (ΔP_{tm}), where $P_{tm} = P_{in} - P_{out}$ represents the difference between the pressure inside and outside the vessel wall:

$$C = \frac{\Delta V}{\Delta P_{tm}} \quad (1.1)$$

Because blood vessels are embedded in surrounding tissues, the overall distensibility measured in vivo is the total compliance C_{tot} , which combines vascular compliance C_v and extravascular (tissue) compliance C_{ev} [20]:

$$\frac{1}{C_{tot}} = \frac{1}{C_v} + \frac{1}{C_{ev}}.$$

Throughout both the respiratory and cardiac cycles, the IVC diameter is influenced by changes in transmural pressure. During the respiratory cycle, the diaphragm contracts during inspiration lowering intrathoracic pressure and raising intra-abdominal pressure, which leads to transient changes in IVC diameter. This respiratory variation is essential for venous return dynamics and can be assessed to evaluate fluid responsiveness in clinical settings. For a detailed explanation of how respiration specifically impacts the IVC, refer to Section 1.2.3.

Additionally, throughout the cardiac cycle, cyclic pressure fluctuations in the right atrium modulate venous inflow and influence the diameter of the IVC [7]. During atrial systole, just before atrial contraction, the development of negative pressure in the right atrium causes a transient narrowing of the IVC as blood is rapidly drawn into the heart. In contrast, during atrial diastole (which coincides

with ventricular systole), the right atrium relaxes and passively fills with blood, allowing the IVC to distend and accommodate increased venous return.

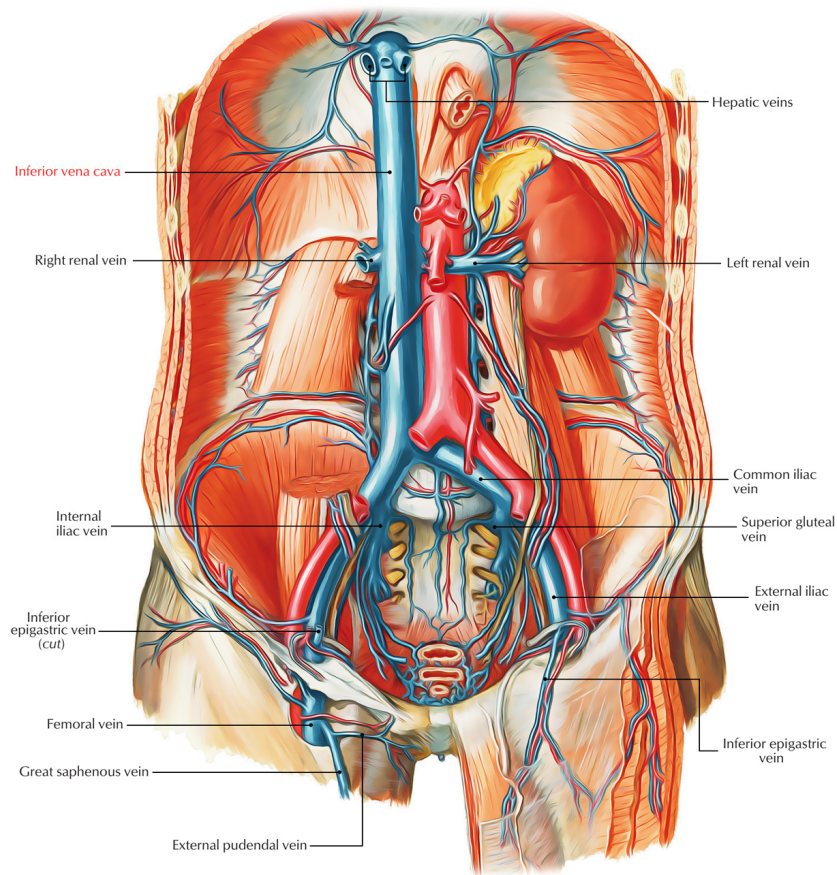


Figure 1.5: Anatomy of the IVC and adjacent structures.

1.1.6 Blood Volume Regulation and Perfusion

The regulation of blood volume and tissue perfusion is a vital function of the cardiovascular system, to guarantee an adequate supply of oxygen and nutrients to all tissues while preserving hemodynamic stability. Blood volume is composed of plasma and cellular components, and its distribution changes across various compartments in response to physiological demands.

While blood is a component of the cardiovascular system, it is not directly regulated by it. Instead, the cardiovascular system maintains arterial pressure, which is essential for adequate tissue perfusion. Changes in blood volume are sensed indirectly through variations in arterial pressure: a reduction in volume leads to vessel collapse and decreased perfusion pressure. To compensate, the system activates vasoconstriction mechanisms, aiming to restore adequate blood pressure and flow. This process is tightly regulated through interactions between the cardiovascular and renal systems, particularly via the renin-angiotensin-aldosterone system (RAAS)

[32].

Beyond its role in maintaining adequate perfusion, blood volume is involved in regulating plasma osmolality, which reflects the concentration of solutes—primarily sodium—and water in the blood. Osmolality is tightly maintained within a narrow range (275–295 mOsm/kg H₂O) through renal modulation of sodium and water handling [32].

Changes in plasma osmolality produce osmotic movements of water between intracellular and extracellular compartments, with effect on plasma volume. For instance, increased osmolality causes water to come out of cells, increasing the extracellular fluid and intravascular volume. Conversely, decreased osmolality causes water to enter cells, reducing the volume of circulating blood. These fluid changes can significantly increase or decrease blood volume, leading to conditions such as hypervolemia and hypovolemia.

It is important to distinguish between *total blood volume* and *effective circulating volume* (ECV). Total blood volume refers to the total fluid within the vascular compartment, including arteries, capillaries, veins, and cardiac chambers. The effective circulating volume, however, represents the portion of this fluid that is actively perfusing tissues and it is sensed by baroreceptors. Although typically proportional to the volume of extracellular fluid (ECF) and total body sodium, the ECV can dissociate from total volume in certain pathological states.

For instance, in conditions such as hyponatremia or heart failure, the total body fluid may be elevated, yet the effective circulating volume remains low. In this case, baroreceptors signal a hypovolemic state, triggering compensatory neurohumoral responses despite the presence of fluid overload. These mechanisms of volume regulation are controlled by sensory inputs, neural pathways, and hormonal signals, which work together to maintain circulatory homeostasis.

1.2 Principles of Respiratory System

Through the process of respiration, the respiratory system helps the exchange of gases between the body and the external environment. Its primary functions are to supply oxygen to tissues and to remove carbon dioxide, a metabolic waste product. This process consists of four interdependent components. First, pulmonary ventilation facilitates the movement of air between the atmosphere and the alveoli of the lungs. Second, gas diffusion allows oxygen and carbon dioxide to be exchanged across the alveolar-capillary membrane. Third, the transport of gases involves the circulation of oxygen and carbon dioxide within the blood and body fluids to and from peripheral tissues. Finally, regulation of ventilation ensures that respiratory activity adapts to meet the body's metabolic needs. Beyond gas exchange, the respiratory system supports several vital functions: it helps regulate acid-base balance, enables vocalization, defends against inhaled pathogens, facilitates heat and water loss, enhances venous return via the respiratory pump, and activates specific plasma proteins during pulmonary circulation.

1.2.1 Anatomy of the Respiratory System

The respiratory system (Figure 1.6) is composed of structures that transport air from the external environment to the lungs, where gas exchange occurs. Air enters through the upper airways and passes into the conducting zone, which includes the larynx, trachea, bronchi, and bronchioles, which divide further into terminal bronchioles (final component of the conducting zone). This zone serves to warm, humidify, and filter the air but does not participate in gas exchange. The trachea divides into left and right bronchi (*primary bronchi*), which further divide into smaller tubes as *secondary*, *tertiary* and *smaller bronchi*. Once these last tubules become less than 1 mm in diameter, they are called bronchioles [37].

The respiratory zone begins with the respiratory bronchioles and ends in alveoli, small sac-like structures where oxygen and carbon dioxide are exchanged between air and blood. Alveoli are surrounded by a dense capillary network, and together with the alveolar epithelium form the thin respiratory membrane (approximately $0.2\text{ }\mu\text{m}$), which enables efficient gas exchange. The lungs contain about 300 million alveoli, providing a surface area of roughly 100 m^2 [37].

The lungs reside within the thoracic cavity, protected by the rib cage and separated from the abdomen by the diaphragm. Each lung is enclosed by a pleural sac with a small amount of pleural fluid that reduces friction during breathing. The diaphragm and intercostal muscles generate the changes in thoracic volume necessary for ventilation.

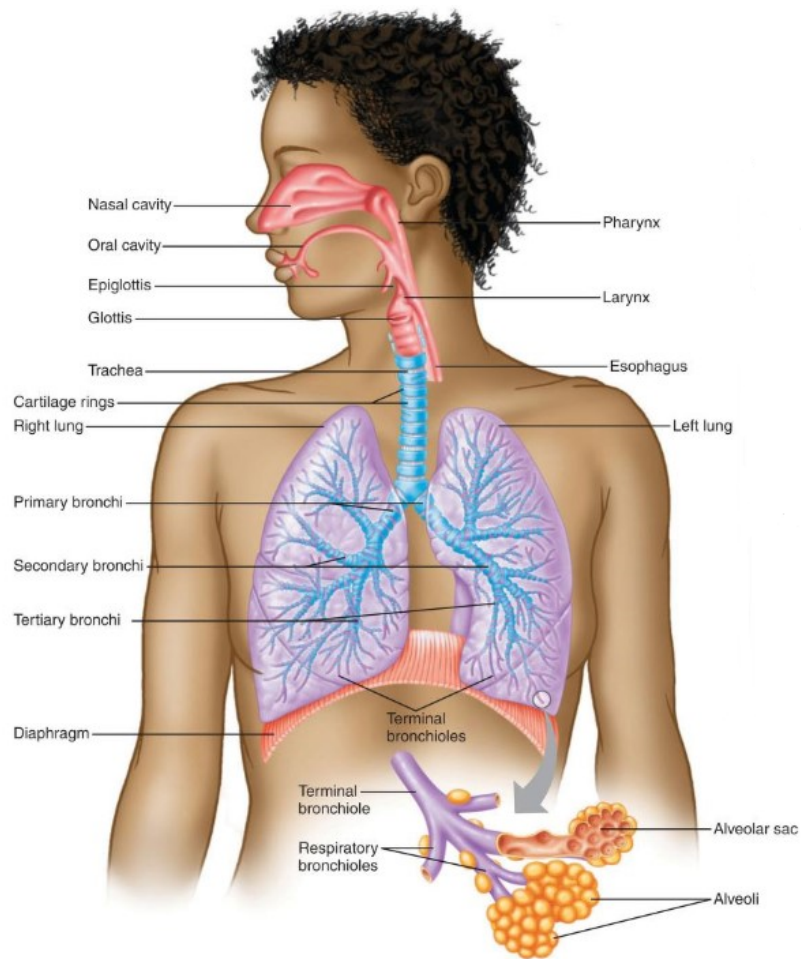


Figure 1.6: Anatomy of the respiratory system

1.2.2 Mechanics of Pulmonary Ventilation

Pulmonary ventilation is driven by changes in thoracic volume through two main mechanisms. The first is the vertical movement of the diaphragm, which contracts and moves downward during inspiration, increasing the vertical dimension of the thoracic cavity and allowing air to enter the lungs. During expiration, the diaphragm relaxes, and the elastic recoil of the lungs, chest wall, and abdominal contents compresses the lungs, pushing air out. This mechanism is the principal driver of quiet breathing. The second mechanism involves the elevation or depression of the rib cage. At rest, the ribs slope downward, but during inspiration, they are lifted, causing the sternum to move forward and increasing the anteroposterior diameter of the chest by approximately 20% during maximal inspiration [7]. The external intercostals are the primary muscles responsible for raising the rib cage during inspiration, while expiration is mainly aided by the abdominal recti and the internal intercostals, which pull the rib cage downward [7].

Ventilation occurs because of pressure gradients between the alveoli and the outside air. Air moves down these gradients, from an area of high pressure to one of

low pressure. Inspiration occurs when the intra-alveolar pressure is less than atmospheric pressure, creating a gradient for air to move into the alveoli. Expiration occurs when intra-alveolar pressure exceeds atmospheric pressure, creating a gradient for air to leave the alveoli. This pressure gradient is influenced by four primary pressures: atmospheric pressure, intra-alveolar pressure, intrapleural pressure, and transpulmonary pressure [37].

Lung expansion depends on the slight negative pressure (pleural pressure) in the pleural cavity, which keeps the lungs adherent to the chest wall. During inspiration, pleural pressure becomes more negative (from -5 to -7.5 cm H₂O), increasing lung volume. Figure 1.7 shows these relationships between the pleural pressure and the change in lung volume. Alveolar pressure falls to about -1 cm H₂O, allowing 0.5 liter of air to enter the lungs in the 2 seconds required for normal inspiration, as shown in Figure 1.7. During expiration, alveolar pressure rises (to about $+1$ cm H₂O), expelling air. The difference between alveolar and pleural pressure is known as transpulmonary pressure. It reflects the elastic recoil force of the lungs and determines how much the lungs expand [7]. Lung compliance refers to the extent to which the lungs expand for each unit increase in transpulmonary pressure and is approximately 200 mL per cm H₂O in healthy adults. It is defined as the change in lung volume (ΔV) divided by the change in transpulmonary pressure ($\Delta(P_{\text{alv}} - P_{\text{pl}})$):

$$\text{Lung compliance} = \frac{\Delta V}{\Delta(P_{\text{alv}} - P_{\text{pl}})} \quad (1.2)$$

This means that a higher lung compliance allows the lungs to expand more easily with a smaller change in pressure, thus requiring less muscular effort during inspiration [37].

Lung compliance can be visualized in the diagram (Figure 1.8) which show the relationship between changes in lung volume and pleural pressure. The shape of the compliance curve is determined by the elastic properties of the lung tissues and the surface tension within the alveoli [7]. Elastic recoil is mainly due to elastin and collagen fibers in the connective tissue of the lungs. When the lungs expand, these fibers resist to stretch generating a recoil force that helps the lungs to return to their resting state. Another factor that helps the lung to resist expansion is the surface tension, created by the thin layer of fluid in the alveoli. Without surfactant to reduce this tension, lung compliance would be lower, and breathing would require much more effort.

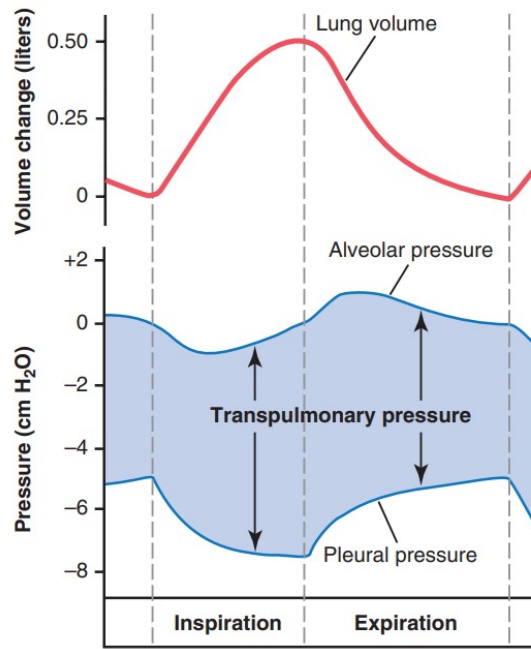


Figure 1.7: The diagram shows the variations in lung volume, alveolar pressure, pleural pressure and transpulmonary pressure occurring during normal respiration.

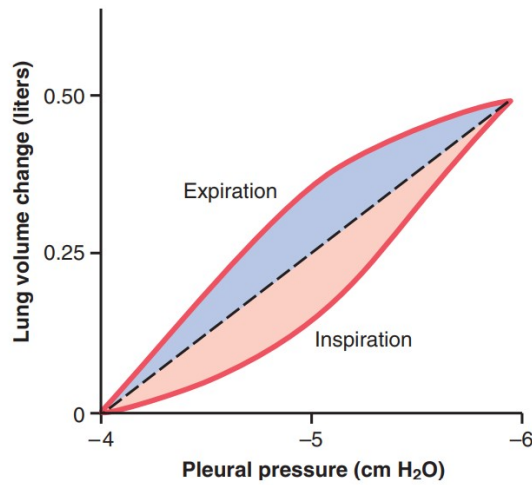


Figure 1.8: Compliance diagram of the lungs.

1.2.3 Respiration effect on IVC

Respiratory activity has a significant influence on the size of the inferior vena cava (IVC) due to the vessel's high compliance and its anatomical position between two dynamic pressure compartments, the thorax and abdomen [5]. The main determinant of IVC size changes is transmural pressure (P_{tm}), defined as the difference

between internal vascular pressure (P_{in}) and external (abdominal) surrounding pressure (P_{out}):

$$P_{tm} = P_{in} - P_{out}, \quad (1.3)$$

According to the non-linear volume–pressure relationship (Figure 1.9) typical of compliant vessels, small changes in P_{tm} at low baseline pressure (e.g., in a normally filled IVC) can lead to large changes in vessel cross-sectional area (CSA). This is because the vessel is highly compliant: the slope of the pressure–volume curve between two points (e.g., from point A to point B) represents compliance, calculated as the change in volume divided by the change in distending pressure. As P_{tm} increases, the compliance of the vein decreases and the curve flattens, meaning further pressure changes yield smaller dimensional variations [20].

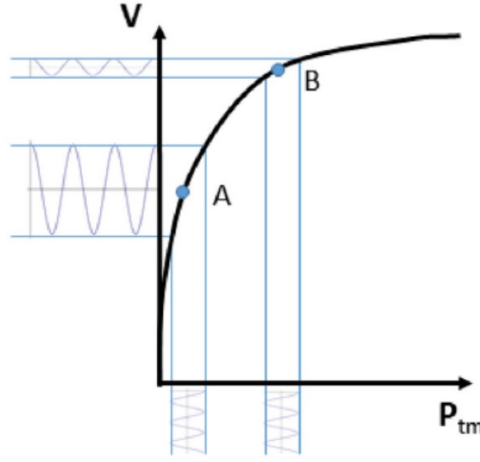


Figure 1.9: Volume - pressure curve of a venous blood vessel, which shows the relationship between the vessel volume (V) and the transmural pressure (P_{tm}).

During the respiratory cycle, the IVC traverses both thoracic and abdominal compartments, so its P_{tm} varies with breathing pattern [5], [20]:

- At end-expiration (*Functional residual capacity, FRC*), intrathoracic and abdominal pressures are balanced, and the IVC reaches its maximum CSA (cross-sectional area).
- During a thoracic inspiration, intrathoracic pressure falls, lowering P_{in} and thus P_{tm} , causing a modest IVC narrowing.
- During diaphragmatic inspiration, the diaphragm descent further raises abdominal pressure (P_{out}), compounding the fall in P_{tm} and producing a much larger decrease in IVC size.
- Under positive-pressure ventilation, intrathoracic pressure rises above baseline, elevating P_{out} and increasing IVC size, the opposite of spontaneous inspiration.

1.3 Principles of Renal Mechanisms of body fluid volume

1.3.1 Body fluid compartments

The total body fluid is distributed mainly in two compartments: the *extracellular fluid* (ECF), which is the fluid outside the cells and account for about 20% of the body weight, and the *intracellular fluid*, which is the fluid inside the cells. The extracellular fluid is divided into the *interstitial fluid* and the *blood plasma* [7]. These two fluids are constantly mixing so they have about the same composition except for proteins, which are more concentrated in the plasma. The plasma proteins have an overall negative charge, which allows them to attract cations such as sodium and potassium ions. These cations are retained in the plasma. On the other hand, negatively charged ions (anions) have a higher concentration in the interstitial fluid, because they are repelled by the negative charges of the plasma. The ECF is characterised by large amounts of sodium and chloride ions and large amounts of bicarbonate ions, but only small quantities of potassium, calcium, magnesium, phosphate, and organic acid ions. The composition of extracellular fluid is regulated by various mechanisms, but especially by the kidneys. The intracellular fluid is separated from the extracellular fluid by a cell membrane that is highly permeable to water but not to most electrolytes in the body. For this reason, in contrast to the extracellular fluid, the intracellular fluid contains only small quantities of sodium and chloride ions but it contains large amounts of potassium and phosphate ions.

1.3.2 Renal regulation of extracellular fluid volume and osmolality

Since sodium is the principal solute in the extracellular fluid, the volume of the ECF is primarily determined by the total amount of sodium in the body [10]. The volume of extracellular fluid (ECF) is controlled by the balance between water and salt intake and excretion. The kidneys play a central role in maintaining body fluid homeostasis by regulating fluid and electrolyte balance. They achieve this by adjusting the excretion of water and sodium to match intake, thereby ensuring that ECF volume remains stable under normal conditions [37].

When changes occur in sodium and fluid intake, a feedback mechanism helps maintain sodium and fluid balance and minimizes significant alterations in blood volume, extracellular fluid (ECF) volume, and arterial pressure. An increase in fluid intake (assuming that it is accompanied by sodium) beyond the rate of urinary excretion causes a temporary accumulation of fluid in the body. Excess fluid accumulates in the blood and interstitial spaces when fluid intake exceeds urine output, leading to parallel increase in extracellular fluid volume and blood volume [7].

However, the actual increases in these variables are typically small, due to the efficiency of the following feedback system:

1. Blood volume rises, increasing the mean systemic filling pressure, which determines how much blood returns to the heart.
2. This improves the pressure gradient for venous return, bringing more blood back to the heart.
3. As a result, cardiac output increases, pumping more blood into the circulation.
4. Higher cardiac output leads to an increase in arterial pressure.
5. Elevated arterial pressure activates pressure diuresis, a process where the kidneys increase urine production in response to the higher pressure.
6. This increased fluid excretion balances the higher intake, stopping further fluid accumulation.

The opposite sequence occurs when fluid intake drops below normal levels. In this case there is a tendency for blood volume and extracellular fluid (ECF) volume to decrease, accompanied by a reduction in arterial pressure. Even a slight drop in arterial pressure triggers a significant reduction in urine output, allowing the body to conserve water and maintain fluid balance. This feedback mechanism ensures that even when fluid and sodium intake fluctuate, the body can efficiently regulate fluid levels avoiding significant changes in blood volume or blood pressure [7].

In addition to intrinsic renal mechanisms such as pressure natriuresis and pressure diuresis, the regulation of extracellular fluid (ECF) volume and osmolarity is strongly influenced by neural and hormonal factors. Nervous and hormonal mechanisms work together with the intrinsic renal mechanisms, making them more effective in minimizing the changes in blood volume, extracellular fluid volume, and arterial pressure that arise during everyday physiological challenges. However, dysfunction in kidney function or in the various nervous and hormonal factors that influence the kidneys can cause significant.

- **Renin–Angiotensin–Aldosterone System (RAAS):** This system is activated when extracellular fluid volume or blood pressure decreases. Its main function is to help retain sodium and water, thereby restoring fluid balance and maintaining blood pressure. The hormone angiotensin II causes blood vessel constriction and stimulates sodium reabsorption in the kidney tubules. It also promotes the release of aldosterone, which further increases sodium reabsorption in the final segments of the nephron. Together, these effects reduce urinary excretion and help stabilize body fluid volume [7].
- **Sympathetic Nervous System:** In response to hypovolemia or hypotension, reflex activation of the sympathetic nervous system leads to renal vasoconstriction. It also enhances sodium and water reabsorption, particularly in the proximal tubule, and stimulates renin release thereby amplifying RAAS activation [7, 10]. These effects promote fluid retention and help restore circulatory volume.

- **Atrial Natriuretic Peptide (ANP):** Released by the heart in response to increased blood volume, ANP promotes the excretion of sodium and water by increasing glomerular filtration and reducing sodium reabsorption in the collecting ducts. This helps correct volume overload. However, its role is relatively limited, as its effects are often overridden by more powerful mechanisms such as pressure natriuresis [7, 10].
- **Antidiuretic Hormone (ADH) and Osmoreceptor Feedback System:** Osmoreceptors in the hypothalamus detect changes in plasma osmolarity and regulate the release of the antidiuretic hormone (ADH). When extracellular fluid becomes hyperosmolar, ADH secretion increases, which causes water reabsorption, thereby diluting the ECF. Conversely, when the ECF is hypoosmolar, ADH secretion decreases, allowing water excretion. ADH helps to conserve water and maintain blood pressure during dehydration [7, 10].
- **Thirst Mechanism:** Controlled by hypothalamic osmoreceptors and low-pressure baroreceptors, thirst is stimulated when plasma osmolarity rises or blood volume decreases. This response promotes increased water intake, helping to restore fluid balance and maintain proper extracellular fluid volume [7].

1.3.3 Disorders of Fluid Volume Regulation: Hyponatremia

The kidneys, through their countercurrent mechanism, concentrate or dilute urine as needed. They balance sodium and water excretion to maintain osmolarity. Hypothalamic osmoreceptors monitor serum sodium levels and regulate antidiuretic hormone (ADH) secretion, ensuring that water re-absorption is adjusted to maintain sodium balance. A defect in the urine-diluting capacity coupled with excess water intake leads to hyponatremia [10].

Hyponatremia is defined as plasma sodium concentration < 135 mEq/l and is the most common electrolyte disorder encountered in clinical practice and may occur in up to 15% to 25% of hospitalized patients [26, 30]. The decrease in plasma sodium concentration reflects a low plasma osmolarity, also designated as hypotonicity. The underlying cause of hypotonic hyponatremia is a disturbance in the urinary diluting mechanism, which it can be disrupted as to impair water excretion, causing its retention and culminating in hyponatremia [10]. Hyponatremia may be caused by loss of sodium chloride from the extracellular fluid or addition of excess water to the extracellular fluid [7].

In clinical practice it is helpful to view disorders of ECF volume as they reflect gain or loss of electrolyte-free water, typically resulting in changes in plasma osmolarity (hyponatremia). Since more than 90% of the solute in the extracellular fluid is composed by sodium and its associated anions (mainly chloride), plasma sodium concentration is a fair indicator of plasma osmolarity under many conditions [7]. Since, as mentioned earlier, sodium is the major solute of extracellular fluid (ECF) the causes of hyponatremia can be classified based on the volume status of the ECF.

Based on the volume of ECF, a patient can be classified into hypovolemic, euvoletic, or hypervolemic [26].

Hypovolemia

It refers to hyponatremia associated with decreased total body sodium. A patient with hypovolemic hyponatremia is characterized by a reduction in total body sodium and water, with sodium loss exceeding water loss. It typically occurs in conditions involving significant gastrointestinal or renal fluid loss, followed by intake of free water or hypotonic fluids. The underlying mechanism is the nonosmotic release of AVP stimulated by volume contraction. This persistent AVP secretion promotes water retention despite hypotonic state, thereby contributing to hyponatremia [10].

Hypervolemia

It refers to hyponatremia associated with increased total body sodium. However, if the water increases more than the sodium, the sodium becomes diluted in the blood, leading to hyponatremia, even though the total amount of sodium in the body is actually higher than normal. This condition typically occurs in case of cardiac failure, cirrhosis, or nephrotic syndrome. These conditions impair free water clearance due to neurohormonal activation leading to water and sodium retention [10]. Disorders associated with hypervolemic hyponatremia all manifest edema formation due to renal sodium and water retention [11].

Euvoletic

It refers to hyponatremia associated with normal total body sodium. These patients have no physical signs of increased or decreased total body Na^+ . This condition is frequently associated with water retention that dilutes sodium concentration in ECF, leading to hyposmotic overhydration. The most common cause of hyponatremia is the inappropriate secretion of antidiuretic hormone (ADH). The syndrome of inappropriate ADH secretion (SIADH) causes AVP to be inappropriately stimulated, leading to urine concentration. Water is retained resulting in hyponatremia even in the absence of sodium loss [10].

1.3.4 Diagnostic approach to patients with Hyponatremia

Hyponatremia is not a disease itself, but rather a manifestation of impaired water homeostasis due to a wide range of underlying pathophysiological mechanisms [9]. As such, accurate classification is essential to guide diagnosis and treatment. The initial step is to differentiate hypotonic from non hypotonic hyponatremia, because treatment strategies differ substantially depending on the underlying tonicity. Hypotonic hyponatremia is then differentiated also on the basis of urine osmolality, urine sodium level, and volume status [9].

So in order to evaluate this condition, clinicians rely on three key parameters:

- **Serum Sodium Concentration** (Natrema): Serum Sodium Concentration is useful to indicate the presence of hyponatremia. A concentration below 135 mEq/L indicates hyponatremia.
- **Plasma Osmolality**: Measurement of plasma osmolality is critical for distinguishing between different types of hyponatremia. Hyponatremia can be divided into two main categories based on serum osmolality: hypotonic and non-hypotonic [23]. Normal plasma osmolality is around 275 mOsm/kg to 290 mOsm/kg (isotonic hyponatremia). In case of hypertonic hyponatremia, serum osmolality gets greater than 290 mOsm/kg. hypotonic hyponatremia is characterised by serum osmolality of less than 275 mOsm/kg [26]. Hypotonic hyponatremia is the most common form, characterized by reduced plasma osmolality due to excess free water relative to sodium [23].
- **Urinary Osmolality**: Measuring urinary osmolality provides insight into the kidney's response to water load. Low urinary osmolality (<100 mOsm/kg) indicates an appropriate renal response, as seen in conditions like primary polydipsia, where the kidney effectively excretes free water [26, 8]. High urinary osmolality (>100 mOsm/kg) suggests an inappropriate renal response, typically due to excess ADH secretion, as in the syndrome of inappropriate ADH secretion (SIADH), or other conditions impairing free water clearance [26, 8].

After evaluating plasma and urinary osmolality, assessing extracellular fluid (ECF) volume becomes the next step. This classification divides hypotonic hyponatremia into hypovolemic, euvoletic, and hypervolemic subtypes [10]. However, traditional volume status assessment by clinical examination is imprecise, with studies reporting sensitivities of 50–80% and specificities as low as 30–50% [9]. Consequently, both U.S. and European guidelines acknowledge the limitations of this method, especially in differentiating hypovolemic from euvoletic hyponatremia, which often lack clear physical findings. Hypervolemic hyponatremia, on the other hand, is more readily identified by the presence of peripheral edema or ascites [9].

To improve diagnostic accuracy, recent European recommendations [35] emphasize the early use of laboratory parameters such as urine osmolality (UOsm) and urine sodium (UNa), rather than relying primarily on clinical volume assessment. A UNa <30 mmol/L typically suggests hypovolemia or hypervolemia due to effective arterial blood volume depletion, while values >30 mmol/L support euvoletic causes such as SIAD. However, interpretation must consider several confounders: low dietary sodium intake, recent diuretic use (which can falsely elevate UNa), and impaired sodium reabsorption in chronic kidney disease (CKD). CKD also complicates water balance assessment by limiting free water clearance and modulating vasopressin responses [9].

In summary, a structured diagnostic approach based on serum sodium, plasma and urinary osmolality, and extracellular fluid volume is essential for classifying

the type of hyponatremia and guiding targeted treatment strategies. Despite the support of established guidelines, clinical evaluation of volume status remains challenging, prompting interest in more objective tools. In the following chapter, we will explore current advances in the management of hyponatremia, with particular focus on the emerging role of inferior vena cava (IVC) assessment in evaluating volemic status.

Chapter 2

Emerging Techniques for Indirect Assessment of Volume Status in Patients with Hyponatremia

The diagnostic classification of hyponatremia, into hypovolemic, euvolemic, or hypervolemic subtypes, relies heavily on the accurate evaluation of a patient's extracellular fluid (ECF) volume. Traditionally, this assessment has been based on the clinical history, physical examination, and laboratory parameters such as serum urea, creatinine, uric acid, and urine sodium concentration. In equivocal cases, the response to isotonic saline infusion is often used to differentiate between hypovolemia and euvolemia (e.g. SIADH). Additionally, biomarkers such as brain natriuretic peptide (BNP) or its inactive fragment NT-proBNP have been integrated into routine practice to help identify fluid overload [11]. However, all of these methods, clinical, laboratory, and biochemical, are often unreliable, particularly in complex or overlapping syndromes.

In recent years, the need for more objective and reproducible tools to estimate volume status has driven the development of several instrumental, non-invasive techniques. These methods aim to provide an indirect assessment of volume status, independent of traditional clinical signs and biochemical markers. Among the most promising are point-of-care ultrasound (PoCUS), including Lung Ultrasound (LUS), Focused Cardiac Ultrasound (FoCUS), Inferior Vena Cava (IVC) Ultrasound and the Venous Excess Ultrasound Score (VExUS), as well as other investigational modalities such as bioimpedance analysis and relative blood volume monitoring.

2.0.1 Bioimpedance

Bioelectrical Impedance Analysis (BIA) has emerged as a promising, non-invasive, and cost-effective technique for assessing hydration status, including extracellular fluid (ECF) volume. Initially developed in the 1980s for nutritional assessment, BIA has progressively gained clinical relevance in broader applications such as chronic kidney disease and hemodialysis (HD), where precise volume management is critical

[3].

The technique is based on the principle that the electrical conductivity of body tissues varies with fluid content. Low-frequency currents predominantly travel through extracellular water (ECW), while high-frequency currents can penetrate both extracellular and intracellular compartments. By measuring the resistance (impedance) and reactance of body tissues to these currents, BIA enables estimation of body fluid distribution and total body water.

BIA is available in several technical configurations:

- Single-frequency BIA: This simpler and more affordable method uses a fixed-frequency current to estimate fluid shifts. Although useful for detecting relative changes in hydration, it cannot provide accurate quantification of individual fluid compartments.
- Multiple-frequency BIA (also called bioimpedance spectroscopy, BIS): This technique uses a spectrum of frequencies to analyse both ECW and intracellular water (ICW), making it more accurate and suitable for clinical fluid assessments, particularly in nephrology.
- Whole-body and segmental BIA: Whole-body analysis assumes that tissue properties are homogeneous, while segmental BIA analyse specific body regions. Segmental methods can be more practical but may reduce accuracy due to anatomical variability in tissue composition.

Although BIA has been widely validated in dialysis and heart failure populations, recent studies [13], [15] have explored its application in patients with hyponatremia, particularly for differentiating hypovolemia from hypervolemia, two conditions that require vastly different therapeutic approaches.

Bioimpedance spectroscopy (BIS) has been shown to correlate well with standard clinical assessments and echocardiographic evaluations of volume status in hyponatremic patients. In one study, BIS effectively distinguished between hypovolemic and hypervolemic hyponatremia, demonstrating good agreement with conventional methods, which were the combination of echocardiography, serum and urine osmolality biochemical tests, and physical examination [15]. Another investigation suggested that BIS could serve as a reliable alternative to clinical volume assessment, reducing the subjectivity associated with physical signs, which are often non specific or absent [13].

These findings suggest that BIA could be an adjunct tool in the traditional diagnostic tools for hyponatremia, but still require further validation before it can be integrated into routine hyponatremia algorithms.

2.0.2 Point-of-Care Ultrasound (PoCUS)

Point-of-care ultrasound is increasingly recognized as a valuable tool in internal medicine and nephrology for the rapid bedside assessment of volume status. It is

a non-invasive test that uses mobile ultrasound technology, often at the patient's bedside [4]. Unlike traditional physical exam findings, which are often subjective and of limited sensitivity, PoCUS provides objective and reproducible parameters related to intravascular and interstitial fluid status. When interpreted in conjunction with the clinical context, provides a valuable adjunct to improve diagnostic accuracy. A variety of POCUS modalities can be applied in assessing volume status, each contributing unique diagnostic insights. These include IVC ultrasound, lung ultrasound, FoCUS, and the more comprehensive VExUS grading system. Each modality evaluates different aspects of the patient's hemodynamic profile. Conceptually, this goal-directed sonographic approach can be summarized as the evaluation of the pump, pipes, and leaks: FoCUS assesses cardiac function ("the pump"), IVC ultrasound and venous Doppler evaluate the venous system and intravascular volume ("the pipes"), while lung and abdominal ultrasound detect extravascular fluid accumulation ("the leaks") [14].

Lung Ultrasound (LUS)

LUS evaluates extravascular lung water and is useful for detecting pulmonary congestion. It distinguishes between a "dry" lung pattern, characterized by horizontal A-lines, and a "wet" lung pattern, identified by vertical B-lines that correlate with interstitial or alveolar fluid accumulation.

- **A-line pattern:** Typically found in normovolemic or hypovolemic patients [17]. These horizontal lines suggest well-aerated lung fields and the absence of fluid overload.
- **B-line pattern:** Vertical lines originates from the pleural line and move with respiration, indicating interstitial edema or pulmonary congestion. In dialysis patients, the number of B-lines is directly proportional to fluid overload and correlates with inferior vena cava (IVC) measurements.

Although not specific to hyponatremia, LUS can assist in differentiating between euvolemic and hypervolemic states in diagnostically ambiguous cases. The detection of multiple bilateral B-lines correlates with increased extravascular lung water and can support the diagnosis of volume overload [24]. However, B-lines have limited specificity and can also appear in a numerous diverse conditions [3]. Furthermore, LUS is not reliable for identifying hypovolemia. Therefore, while LUS is a valuable, easy-to-perform tool with high sensitivity for pulmonary congestion, its interpretation must be integrated with clinical context and other ultrasound parameters to avoid diagnostic misclassification in patients with hyponatremia.

Focused Cardiac Ultrasound (FoCUS)

Focused Cardiac Ultrasound (FoCUS) is a rapid, bedside echocardiographic examination that enables clinicians to assess cardiac function and volume status in real time. FoCUS specifically addresses pump function, using the "5 Es" approach:

Ejection (left ventricular ejection and contractility), Effusion (presence of pericardial fluid), Equality (comparison of right and left ventricular size), Entrance (IVC diameter and collapsibility), and Exit (measurement of the ascending aorta) [28]. A comprehensive assessment with FoCUS requires evaluation of both cardiac structure and function. To improve diagnostic accuracy, clinicians should obtain high quality images from multiple acoustic windows. Standard practice includes acquiring five core views: the parasternal long axis (PLAX), parasternal short axis (PSAX, typically at mid-ventricular level), apical four-chamber (A4C), subcostal four-chamber (S4C), and subcostal IVC view [41]. One particularly useful Doppler-based application of FoCUS is the measurement of left ventricular outflow tract velocity time integral (LVOT VTI). This parameter serves as a surrogate for stroke volume and thus cardiac output. In patients with hyponatremia, a low VTI may indicate hypovolemia. While in cases of suspected hypervolemic hyponatremia, FoCUS may reveal features of congestive heart failure, including reduced ejection fraction, dilated cardiac chambers, or elevated right heart pressures, supporting a diagnosis of volume overload [17]. Furthermore, while FoCUS provides rapid, actionable information, it should not be interpreted in isolation. Integration with clinical, laboratory, and other imaging findings is essential for accurate diagnosis and management.

Venous Excess Ultrasound (VExUS)

The Venous Excess Ultrasound (VExUS) protocol is a Doppler ultrasound based technique, which analyse blood flow in different organs to assess systemic venous congestion, particularly in patients with fluid overload. It combines the evaluation of the inferior vena cava (IVC) with Doppler assessment of flow patterns in the hepatic, portal, and intrarenal veins to produce a semi-quantitative score of congestion [40].

- **Step 1 – IVC assessment:** In the first step the IVC diameter and collapsibility are measured. If the IVC is < 2 cm in diameter and shows respiratory collapsibility $> 50\%$, the patient is unlikely to be congested (VExUS grade 0), and the protocol can be stopped.
- **Step 2 – Hepatic, portal, and renal vein Doppler:** If the IVC is dilated (≥ 2 cm) and shows reduced collapsibility, further evaluation is performed:
 - *Hepatic vein:* Normal flow is biphasic; a reversal of the systolic wave suggests elevated right atrial pressure.
 - *Portal vein:* Normal flow is continuous; pulsatility $> 30\%$ or interrupted/reversed flow suggests congestion.
 - *Intrarenal vein:* Continuous monophasic flow is normal; discontinuous or pulsatile flow is pathological.

Each of these Doppler signals is categorized as normal, mildly abnormal, or severely abnormal. The final VExUS grade is determined as follows [2]:

- **Grade 0:** No signs of congestion in any of the three systems.

- **Grade 1:** IVC dilated, with only mild congestion in one system.
- **Grade 2:** Severe congestion in one system.
- **Grade 3:** Severe congestion in at least two systems.

2.0.3 Inferior Vena Cava (IVC) Ultrasound

Although traditionally considered part of Point-of-Care Ultrasound (PoCUS), IVC ultrasound deserves dedicated attention due to its frequent use as a rapid, non-invasive tool to determine volume status. IVC diameter and collapsibility index (CI), measured during the respiratory cycle, have been shown to correlate with right atrial pressure and overall volemia, particularly in emergency and critical care settings. The CI is calculated using the following formula:

$$CI = \frac{IVC_{\max} - IVC_{\min}}{IVC_{\max}}$$

where IVC_{\max} and IVC_{\min} are the maximum and minimum IVC diameters during expiration and inspiration, respectively. In spontaneously breathing patients, inspiration leads to negative intrathoracic pressure, increasing venous return and decreasing IVC diameter. At end-expiration, intrathoracic pressure returns to baseline, reducing venous return and increasing the IVC diameter.

According to the 2010 Guidelines for the Echocardiographic Assessment of the Right Heart in Adults, which is a widely adopted method for interpreting measurement of IVC diameters to estimate relative intravascular volume status [12], [27]:

- IVC diameter < 2.1 cm with $> 50\%$ collapse during a sniff suggests normal mean right atrial pressure (RAP) of 0–5 mmHg, typically associated with euvolemia or hypovolemia.
- IVC diameter > 2.1 cm with $< 50\%$ collapse during a sniff suggests elevated RAP of 10–20 mmHg, suggestive of hypervolemia or elevated right-sided filling pressures.

Its application still presents some limitations: the IVC diameter is influenced not only by intravascular volume status, but also by factors such as respiratory mechanics, right heart function, and variations in intra-abdominal or intrathoracic pressures. Furthermore, technical challenges, such as poor acoustic windows in patients with obesity, bowel gas, or mechanical ventilation, can impair image acquisition. Operator dependency is another well-recognized issue; ultrasonographic measurements of IVC can vary based on the examiner’s experience and technique, leading to potential interobserver variability [3].

Despite its widespread application in conditions such as shock, sepsis, and heart failure, IVC ultrasound has been rarely studied in isolation in the context of hyponatremia. In fact, most clinical protocols and studies incorporate IVC assessment

within broader multi-organ frameworks like FoCUS or VExUS, rather than evaluating it as a standalone diagnostic modality.

The study by Şirin et al. [33] is one of the few to specifically investigate the role of inferior vena cava (IVC) ultrasound in patients with hyponatremia. While supporting previous findings on the utility of IVC collapsibility index (CI) in volume assessment, this study focused on its application in the context of hyponatremia. The authors demonstrated that respiratory variation in IVC diameter, measured in terms of CI, was associated with the classification of patients into hypovolemic, euvolemic, and hypervolemic groups [33]. Their findings suggest that a CI greater than 50% indicates hypovolemia, while a CI below 20% is more consistent with hypervolemia. This study highlights the potential of IVC ultrasound as a valuable tool in the diagnostic algorithm of hyponatremia.

2.0.4 Summary and Clinical Relevance

In clinical practice, hyponatremia is often approached through an empirical combination of physical examination, laboratory tests (including serum and urine sodium, BUN, and uric acid), and therapeutic trials (e.g., isotonic saline). However, these methods may fail to provide definitive answers, especially in patients with comorbid conditions like CKD, heart failure, or liver cirrhosis.

Emerging technologies such as Point-of-Care Ultrasound (PoCUS), particularly Lung Ultrasound (LUS), Focused Cardiac Ultrasound (FoCUS), and the Venous Excess Ultrasound Score (VExUS), offer a bedside, non-invasive assessment of volume status. These modalities can serve as valuable adjuncts in the diagnostic and therapeutic management of hyponatremia, as they help identify patterns of pulmonary edema, cardiac dysfunction, or systemic venous congestion that may not be evident through physical examination or standard laboratory tests. Although originally developed for other clinical contexts, their application in the evaluation of hyponatremia is increasingly supported by clinical evidence and expert consensus [4], [25], [28], [17], [29].

Nevertheless, these techniques are not without limitations. In particular, VExUS requires high-quality Doppler images from multiple abdominal veins, which may be technically challenging in certain patients. Operator dependency, suboptimal acoustic windows, and variability in interpretation can limit reproducibility. Similarly, FoCUS requires a minimal level of echocardiographic skill to acquire and interpret standard views reliably. Therefore, PoCUS should be viewed as a valuable complement, not a replacement, for clinical judgment and comprehensive assessment. As training and standardization improve, its role in the management of hyponatremia is likely to expand further.

Chapter 3

Principles of Ultrasound

Ultrasound imaging is a non-invasive diagnostic technique that utilizes high-frequency sound waves to generate real-time images of internal body structures. This modality has gained widespread use in clinical practice due to its safety, accessibility, and ability to provide dynamic imaging without exposing patients to ionizing radiation. The fundamental principle of ultrasound imaging is based on the interaction of sound waves with body tissues, specifically through reflection and scattering phenomena. Ultrasound waves are mechanical compression and rarefaction waves, characterized by key physical parameters such as frequency and wavelength, which directly influence image resolution. Higher frequencies provide better spatial resolution but are associated with greater attenuation, limiting penetration depth.

- **Propagation Velocity (m/s):** the speed at which sound travels, is determined by the medium's stiffness and density. Following the equation:

$$v = \lambda \cdot f \quad (3.1)$$

where v is velocity, λ is wavelength, and f is frequency. In biological tissues, the average speed of ultrasound is approximately 1540 m/s, but it varies across different media, being highest in dense, non-elastic tissues such as bone (4080 m/s) and lowest in lipid-rich tissues like adipose tissue (1460 m/s).

- **Acoustic impedance (Pa·s/m³):** it represents the resistance that a medium opposes to the propagation of a sound wave. It depends on both the density of the medium and the propagation velocity of ultrasound through the medium, according to the equation:

$$Z = \rho \cdot v \quad (3.2)$$

where Z is the acoustic impedance, ρ is the density of the material and v is the speed of the ultrasound. A high impedance value indicates that the medium provides greater resistance to the passage of the sound wave, while a low impedance value means lower resistance.

The acoustic impedance determines how much of the ultrasound wave is transmitted or reflected at the interface between different tissues. The reflection coefficient (R) quantifies this effect and is given by:

$$R = \left(\frac{Z_1 \cos \alpha_2 - Z_2 \cos \alpha_1}{Z_1 \cos \alpha_2 + Z_2 \cos \alpha_1} \right)^2 \quad (3.3)$$

By definition, this coefficient varies between 0 and 1.

In clinical ultrasound, the most relevant scenario is normal incidence, where the ultrasound wave strikes the interface between two media perpendicularly (α_1). Under these conditions, the reflection coefficient simplifies as:

$$R = \left(\frac{Z_2 - Z_1}{Z_2 + Z_1} \right)^2 \quad (3.4)$$

If the acoustic impedances of the two media are nearly identical, the reflection coefficient approaches zero, meaning that almost all the ultrasound wave is transmitted. In this case, there is minimal reflection, leading to poor echo signal reception, which can impact detectability in ultrasound imaging.

If the two media have very different acoustic impedances, the reflection coefficient is close to 1, indicating that almost all of the ultrasound wave is reflected and almost none is transmitted. This phenomenon blocks the transmission of the ultrasound beyond the interface, which make deeper structures inaccessible. This is particularly problematic in case of bone or air containing regions, since bone has a very high acoustic impedance, while air has an extremely low acoustic impedance compared to soft tissues. In abdominal ultrasound, for example, the presence of intestinal gas (air) can block ultrasound wave transmission, reducing image quality.

When a sound beam reaches the interface between two mediums with different acoustic impedances, some of it passes through the interface and its direction is changed. This is called refraction. The amount of refraction is proportional to the difference in the velocity of sound in the two tissues and to the angle of incidence. This is explained by the *Snell's Law* (Figure 3.1) as follows:

$$\frac{n_2}{n_1} = \frac{\sin \theta_1}{\sin \theta_2} \quad (3.5)$$

where n_1 is the incident index and n_2 is the refractive index, θ_1 is the incident angle and θ_2 is the refracted angle. Refraction can cause the ultrasound beam to change direction, potentially leading to artifacts or distortions in the final image.

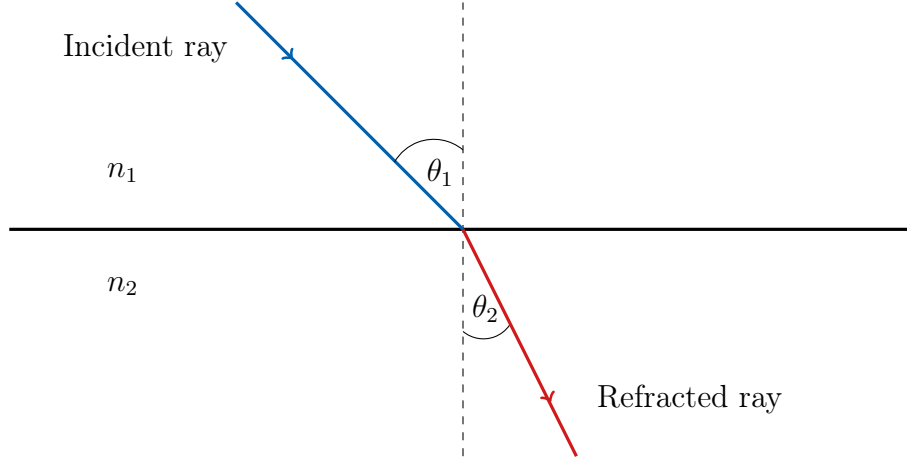


Figure 3.1: Illustration of Snell's Law.

An important factor that affects ultrasound imaging is attenuation, which is the progressive loss of energy as the ultrasound propagates through biological tissues. This energy loss occurs because of absorption and scattering, which lead to a decrease in signal intensity as it penetrates deeper in the tissues. This phenomenon is described by the following formula:

$$A(z) = A_0 \cdot e^{-\alpha z} \quad (3.6)$$

where α is the absorption coefficient, which is directly proportional to frequency. Higher frequencies enhance axial resolution but they also lead to greater attenuation, limiting the imaging depth.

Time gain compensation (TGC) is implemented in ultrasound systems to compensate this effect. This technique allows to adjust signal amplification at different depths to maintain uniform image brightness and prevent signal loss in deeper structures. TGC acts as a logarithmic amplifier that increases the gain based on the travel time of the echo. As a result, echoes from deeper tissues, which are more attenuated due to longer propagation, are displayed with similar intensity as superficial ones.

Ultrasound waves are produced by piezoelectric crystals, typically made of lead zirconate titanate (PZT), which exploit the inverse piezoelectric effect: an applied electric voltage induces mechanical deformation, producing acoustic waves. Conversely, the returning mechanical waves deform the crystals (direct piezoelectric effect), generating electrical signals that are processed into diagnostic images.

Modern ultrasound transducers work as both transmitters and receivers. By measuring the time between the emission of an ultrasound pulse and the return of its echo, and using the known propagation velocity in the medium, it is possible to calculate the depth of the reflecting structure. This principle is the foundation of ultrasound imaging.

The distance to a reflecting interface is calculated by measuring the round-trip time of flight (Δt) of the pulse, using the formula:

$$d = \frac{1}{2}c \cdot \Delta t \quad (3.7)$$

where c is the speed of sound in soft tissue (approximately 1540 m/s).

The wavelength of the emitted ultrasound is inversely related to the thickness of the piezoelectric elements within the transducer, following:

$$f = \frac{c}{2h} \quad (3.8)$$

where f is the resonance frequency, h is the crystal thickness, and c is the speed of sound in the transducer material. Thinner elements produce higher frequencies, which offer improved resolution but reduced penetration due to increased attenuation.

The ultrasound beam has a specific geometric profile: it is relatively narrow in the near field (Fresnel zone) and diverges in the far field (Fraunhofer zone). The near field length is calculated as:

$$L_n = \frac{D^2}{4\lambda} \quad (3.9)$$

where D is the transducer diameter and λ is the wavelength. A larger transducer and higher frequency (shorter λ) result in a longer near field and narrower beam width. This results in better spatial resolution.

To further improve image quality, the beam can be focused at a specific depth, known as the focal zone. This increases lateral resolution and contrast, and can be achieved mechanically or electronically.

Due to the three-dimensional shape of the ultrasound field (typically fan-shaped or pyramidal), spatial resolution is defined in three directions:

- *Axial resolution*, along the beam propagation direction, primarily influenced by pulse length;
- *Lateral resolution*, perpendicular to the beam in the image plane, dependent on beam width and focusing;
- *Elevation resolution*, perpendicular to the image plane, influenced by the transducer's geometry and design.

Axial resolution is critical in diagnostic imaging. It is directly proportional to both the wavelength and the pulse length, and is typically limited to 2–3 times the wavelength. In modern systems the emitted pulses consists of 2–3 sinusoidal cycles. Shorter pulses improve axial resolution but reduce imaging depth due to increased attenuation. This introduces a trade-off between resolution and penetration.

Multifrequency transducers are used to accomodate different clinical needs. These devices can operate over a bandwidth centered around a chosen frequency and allow adjustment of resolution and depth. The transducer alternates between emission and reception modes to capture the returning echoes, which are then processed to build the final image.

3.1 Ultrasound Probes and Imaging Modalities in Diagnostic Applications

In diagnostic ultrasound, the choice of probe and visualization mode is determined by the anatomical target, required resolution, and depth of investigation. This section outlines the principal ultrasound modalities and probe types used.

Imaging Modalities

There are three imaging modes in ultrasound diagnostics: A-mode, B-mode, and M-mode.

- **A-mode (Amplitude Mode):** A-mode is the most basic ultrasound modality. It uses a single transducer and the echoes are displayed as vertical spikes along a baseline, where depth is represented along the horizontal or vertical axis (depending on orientation) and amplitude corresponds to echo intensity. This mode provides accurate one dimensional measurements but it has limited spatial imaging capability.
- **B-mode (Brightness Mode):** B-mode is the standard imaging modality used in clinical ultrasonography. It produces a two-dimensional grayscale image in which the brightness of each pixel represents the echo amplitude and the position is determined by the time of flight and the angle of the beam. The final image consists of multiple adjacent scan lines, which form a cross-sectional view of the structure.
- **M-mode (Motion Mode):** M-mode captures motion along a single scan line over time, which is able to transform tissue motion into a temporal graph. It displays depth along the vertical axis and time along the horizontal axis. M-mode offers high temporal resolution.

Ultrasound Probes

Modern ultrasound systems employ electronically controlled transducers composed of multiple piezoelectric elements, arranged in various array configurations (Figure 3.2). These elements are activated in sequences that determine the direction, shape, and focus of the ultrasound beam.

- **Linear Array Probes:** The piezoelectric elements are aligned in a straight line, with elements typically ranging from 128 to 256. These probes operate at high frequencies (5–15 MHz), providing good axial and lateral resolution, which is ideal for superficial structures within 3–4 cm of the skin surface. Since they have a wide footprint, they require a large skin contact area, which make them not suitable for subcostal or intercostal applications.

- **Convex (Curvilinear) Array Probes:** The elements are arranged along a curved arc, typically with a radius of curvature of around 60 mm. The number of elements generally ranges from 100 to 120. Operating at lower frequencies (2–7 MHz), convex probes provide deeper penetration (15–20 cm) at the cost of reduced resolution. The acoustic field diverges in a sector-like fashion, enabling simultaneous visualization of large anatomical areas. These probes are primarily used in abdominal, obstetric, gynecological, and general thoracic imaging.
- **Phased Array Probes:** These probes have a small footprint, typically with 64 to 128 elements, and are capable of electronic beam steering. It is possible to apply a specific timing delays to the excitation of each crystal, in order to direct the emitted ultrasound beam at different angles without moving the probe. This configuration is useful for transthoracic ultrasonography, transcranial Doppler, and pediatric applications where the access is limited but a wide field of view is necessary.
- **Microconvex and Endocavitary Probes:** These are miniaturized convex array probes. Their smaller contact area make them suitable for internal imaging. The emitted field remains divergent, which allows a large field of view within small body cavities. Since the acoustic path is shorter, they typically work at higher frequencies (4–10 MHz), which offer higher resolution in near-field imaging.

Advanced ultrasound machines often support multiple transducers allowing clinicians to switch between different probes.

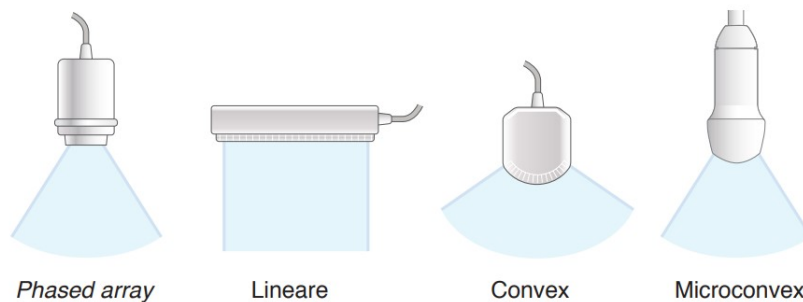


Figure 3.2: Types of probe used in diagnostic

3.2 US Imaging of the IVC

In ultrasound evaluation of the inferior vena cava (IVC) two types of probes are commonly employed based on the clinical setting: a low-frequency convex probe (2–5.5 MHz) is preferred for abdominal imaging, while a phased array transducer (2–8 MHz) is suitable for cardiac applications due to its small footprint and improved maneuverability in subcostal acoustic windows.

3.2.1 IVC Visualization: Longitudinal and Transverse Views

The IVC is most commonly visualized from a subcostal view: the patient lies on the back or slightly turned to the left. The probe is placed just below the sternum and tilted upward toward the heart. In situations where a subcostal window is suboptimal or unavailable, a coronal transhepatic scan along the posterior right axillary line can serve as an effective alternative [1]. The IVC can be assessed in two imaging planes. The longitudinal (long-axis) view, which is most commonly used, offers a clear view of the IVC as it joins the right atrium and allows the visualization of the hepatic veins that flow into it. This setup is ideal for measuring the IVC diameter close to its connection with the heart. In spontaneously breathing patients, the variation of the diameter is likely to be smaller near the right atrium and larger about 2 cm caudal to the hepatic vein confluence. Most authors suggest to acquire these measurements within 1.5 cm from the IVC to the right atrial junction [1]. Alternatively, a transverse (short-axis) view is obtained by rotating the probe 90°, producing a cross-sectional image of the vessel.

3.2.2 Imaging Modalities: B-Mode and M-Mode

B-mode imaging is initially used to identify the IVC, distinguish it from adjacent structures (e.g., aorta, hepatic veins, liver, heart), and assess anatomical continuity with the right atrium, as shown in Figure 3.3a. Proper orientation and use of sufficient gel are essential to minimize reverberation and obtain an artifact-free image. The vessel appears as an anechoic tubular structure, flanked by echogenic walls and respiratory variation in diameter.

Once identified, M-mode (motion mode) is applied perpendicularly to the longitudinal axis of the IVC, typically within 1–2 cm of the atriocaval junction. This modality captures time-dependent changes in vessel diameter over multiple respiratory cycles, as shown in Figure 3.3b. The sweep speed is set between 25 and 50 mm/s, depending on the patient’s respiratory rate, to ensure visualization of at least three full cycles [1]. The resulting IVC waveform demonstrates phasic variation with respiration, collapsing with inspiration in spontaneously breathing patients and distending during positive pressure ventilation.

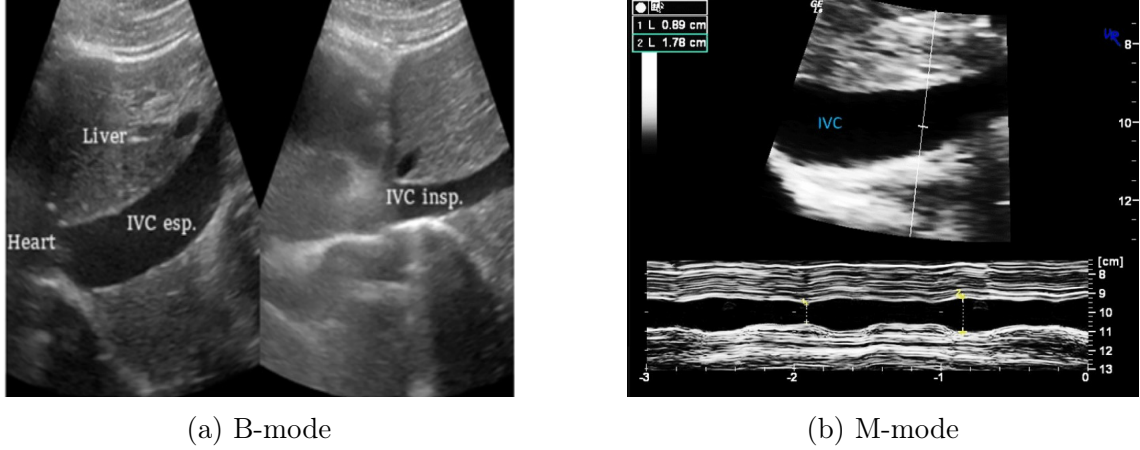


Figure 3.3: Longitudinal scan of IVC taken in two ultrasound modes. (a) B-mode allows to identify the IVC and the adjacent structures; (b) M-mode captures time-dependent changes in vessel diameter along a fixed direction.

3.2.3 IVC-Derived Indices

In inferior vena cava (IVC) ultrasound, two parameters are commonly assessed: the IVC diameter and the Caval Index (CI). The latter is used to describe the variation of the diameter during a respiratory cycle, due to the changes in intrathoracic pressure. Due to its non invasiveness and rapid acquisition, CI is widely used in emergency and critical care settings, particularly for fluid status evaluation and guidance of volume resuscitation. However, studies have shown that IVC pulsatility is not only driven by respiratory dynamics, but also by pressure changes related to cardiac activity. A study [34] show the importance of the cardiac activity on the pulsatility of the IVC. Two additional indices have been proposed, to better distinguish these two physiological components: the Respiratory Caval Index (RCI) and the Cardiac Caval Index (CCI). It is possible to extract the cardiac and respiratory components, by filtering the IVC diameter, in order to allow a more specific assessment of their respective influences on IVC collapsibility.

Chapter 4

Material and Methods

4.1 Scanning Procedure and Equipment

Ultrasound examinations were performed using a Samsung HM70EVO ultrasound system (Figure 4.2) equipped with a convex CA1-7AD transducer (Figure 4.1), operating at a central frequency of 2.5 MHz. This configuration allows for adequate penetration and resolution for abdominal imaging, particularly suited for evaluation of the inferior vena cava (IVC). In the standard imaging approach the transducer was positioned just under the xiphoid process, in the subcostal window. In this view, both longitudinal (long-axis) and transverse (short-axis) scans of the inferior vena cava (IVC) were acquired. In cases where the subcostal view was not optimal, such as in patients with excessive bowel gas, a coronal transhepatic scan was used as an alternative. This view was obtained by placing the transducer in a right intercostal position along the posterior axillary line. All scans were performed with the patient in a supine position in bed. For each patient, at least three ultrasound videos were acquired, each lasting 10 seconds and recorded in B-mode. This duration of acquisition was chosen to ensure the inclusion of at least three complete respiratory cycles per video. The acquisition protocol was designed to allow the assessment of repeatability. The acquisition of multiple recordings for each patient also enabled the selection of the most suitable videos for IVC segmentation in cases of poor visualization, providing redundant data to support a more reliable extraction of the parameters. The recordings were performed in sequence, within the same clinical session, in order to minimize movement artifacts and guarantee temporal consistency between acquisitions.



Figure 4.1: Convex CA1-7AD transducer



Figure 4.2: Samsung HM70EVO ultrasound system

4.2 VIPER

As previously discussed, a widely adopted non-invasive method for assessing intravascular volume status involves evaluating the pulsatility of the inferior vena cava (IVC) diameter using ultrasound (US). This pulsatility is typically quantified through the Caval Index (CI), which reflects the variation in vessel diameter throughout the respiratory cycle. However, respiratory motion induces displacement of the IVC relative to the ultrasound probe, introducing additional variability and potential inaccuracy in pulsatility assessment.

The objective of the developed software, VIPER, is to enable semi-automated tracking of the IVC walls in both transverse (Figure 4.5) and longitudinal (Fig-

ure 4.4) ultrasound views [19, 18]. By accurately delineating the vessel edges across frames, VIPER aims to improve the reliability and reproducibility of IVC-derived metrics, such as diameter measurements and caval indices, thus providing a more robust assessment of vascular pulsatility.

The software, initially developed in MATLAB, was later reimplemented in Python, to enable the real time analysis by interfacing directly with an ultrasound system. The version in Python supports two modes of operation: real-time analysis and offline analysis of pre-recorded ultrasound videos. Both longitudinal and transverse views of the IVC can be processed. In the context of this study, only pre-recorded ultrasound videos were analyzed. At the beginning of the workflow, the user is prompted to select a 5 cm segment on the on-screen graduated scale, which the software uses to calculate the pixel-to-millimeter conversion factor. The sidebar highlighted by the yellow rectangle in Figure 4.3 is used, in which each marking corresponds to 10 mm. Next, the user selects a point along the IVC section in the first frame of the video to define the region of interest for subsequent segmentation and analysis. This point acts as the seed for vessel tracking. Because respiratory motion or patient shifts can displace the IVC relative to its location in the first frame, the software compensates for such movement [22, 19] so that diameter measurements always remain centered on the vein. The position of the reference point is automatically remapped in subsequent frames [19]. Repeating this procedure frame by frame yields a motion compensated series of diameter measurements along the selected IVC segment. For each frame, the diameter is computed as the average distance between the segmented superior and inferior borders along the length of the tracked section, obtaining the estimated diameter time series.



Figure 4.3: The graduated scale on the right indicates intervals of 10 mm per tick mark. The yellow rectangle highlights the sidebar, while the two red dots indicate a 5 cm segment used for the conversion factor.

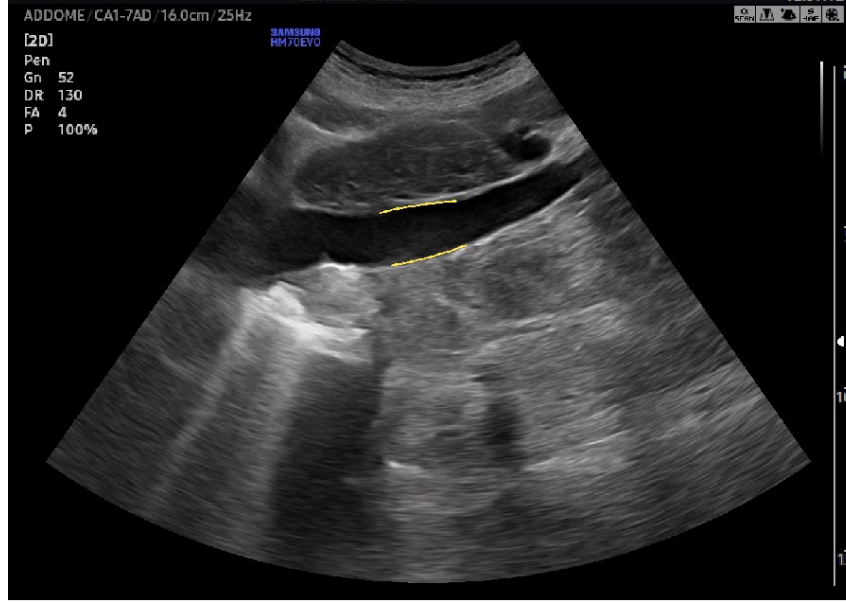


Figure 4.4: Segmentation of the IVC edges in longitudinal view.

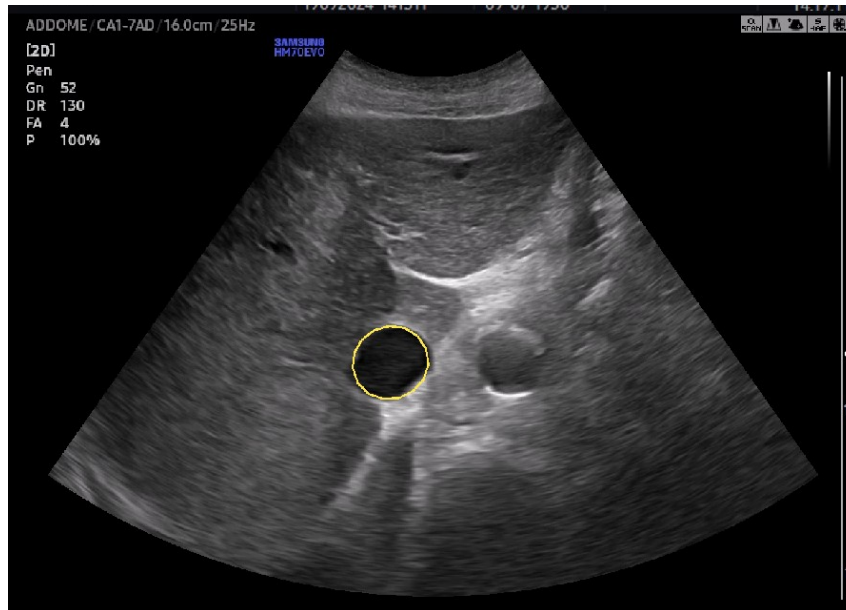


Figure 4.5: Segmentation of the IVC edges in transversal view.

4.2.1 Pulsatility Indices Estimation

Once the time series of IVC diameters has been obtained, whether in longitudinal or transverse view, the next step involves the extraction of pulsatility indices that characterize the mechanical behavior of the vessel across the respiratory and cardiac cycles. The diameter variation over time is influenced by two principal components: a low-frequency respiratory component, due to thoracic pressure changes, and a

higher-frequency cardiac component, induced by right atrial pressure oscillations. To isolate and quantify these effects, specific filtering and signal processing steps are applied. First, the original diameter signal is preprocessed to reduce noise using a Chebyshev Type I low-pass filter with a cutoff frequency of 5 Hz. To extract the respiratory component, the smoothed diameter signal is further filtered with a low-pass Butterworth filter (order 4, zero-phase filtering) with a cutoff frequency of 0.4 Hz. The resulting signal captures the slow oscillations related to respiration (Figure 4.6). Conversely, the cardiac component is isolated by applying a high-pass Butterworth filter with a cutoff frequency of 0.8 Hz to the same preprocessed signal (Figure 4.7). For each component (original, respiratory, and cardiac), the maximum and minimum peaks are detected. These extrema are then used to compute three indices:

- **Caval Index (CI)**: Reflects overall diameter variation and is computed from the estimated diameter time series, using the formula (4.1). Local maxima and minima were computed for each respiration cycle [21].
- **Respiratory Caval Index (RCI)**: Computed using the same formula (4.1), applied to the respiratory component only [21].
- **Cardiac Caval Index (CCI)**: Derived from the cardiac component applying the same formula (4.1) [21].

These indices are calculated frame by frame using the standard formula:

$$\text{Caval Index} = \frac{D_{\max} - D_{\min}}{D_{\max}} \quad (4.1)$$

where D_{\max} and D_{\min} refer to the maximum and minimum peaks.

The signal is averaged over the interval between the first and last valid peaks, excluding edge artifacts, in order to obtain a single representative value per index for each video.

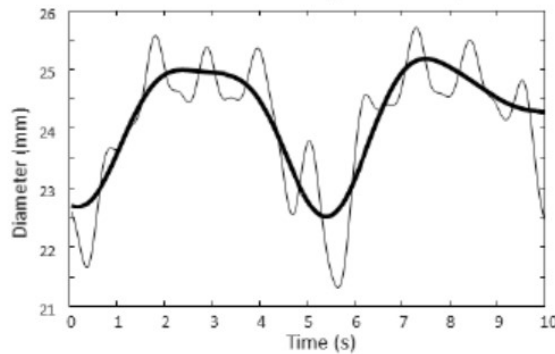


Figure 4.6: IVC diameter over time and respiratory component (highlighted in bold) extracted by filtering.

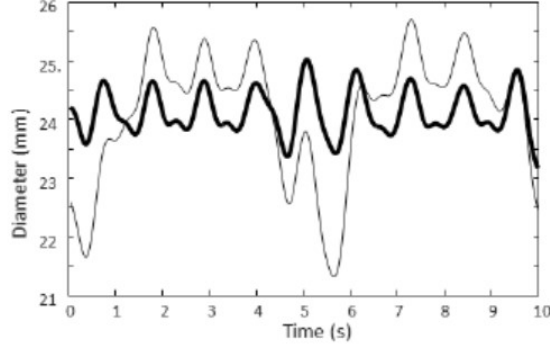


Figure 4.7: IVC diameter over time and cardiac component (highlighted in bold) extracted by filtering.

4.3 Dataset

The study sample consists of 33 hyponatremic subjects, divided into 21 females and 12 males and with an age between 41 and 95 years (mean age 81.45 ± 12.78 years). All patients were diagnosed with hyponatremia at the time of data collection, with serum sodium levels ranging from 116 to 134 mmol/L (mean = 128.77 ± 5.19).

Immediately upon diagnosis, ultrasound video acquisitions were performed. For each patient, three 10s video recordings were collected within seconds of each other to ensure consistency and limit variability due to patient movement or clinical intervention.

Target Class	Number of Patients
0 (Hypovolemic)	6
1 (Euvolemic)	14
2 (Hypervolemic)	13

Table 4.1: Distribution of patients by target class

4.3.1 Clinical and Ultrasound Data

The clinical data available for each patient included the following parameters: age, sex, serum sodium (used only to confirm hyponatremia and excluded from further analysis), plasma osmolality (mOsm/kg), spot urine sodium (mEq/L), urine osmolality (mOsm/kg), ACTH (pg/mL), cortisol (nmol/L), TSH (μ UI/mL), FT4 (pg/mL), renin (μ UI/mL), aldosterone (ng/dL), NT-proBNP (pg/mL), presence of edema, and central venous pressure (PVC).

To complement the clinical dataset, ultrasound features were extracted from three IVC video acquisitions (10 seconds each), per patient using the VIPER software. The extracted parameters included minimum, maximum, and mean diameters and the collapsibility indices (CI, RCI, CCI), derived from both longitudinal and short-axis views.

The serum sodium column was exclusively used to identify hyponatremia and was excluded from subsequent analysis. Variables with more than five missing values (NaNs) were discarded from the dataset. These included: spot urine sodium (mEq/L), urine osmolality (mOsm/kg), ACTH (pg/mL), renin (μ UI/mL), and aldosterone (ng/dL). For the ultrasound-derived parameters, the median value across the three video acquisitions was computed for each patient to reduce redundancy and minimize the impact of potential outliers or noise. Not all ultrasound acquisitions were usable for feature extraction, as some lacked adequate visualization of the IVC, most notably due to the presence of bowel gas, which hindered correct IVC segmentation by the software. In such cases, only the specific acquisitions with insufficient quality were excluded, without discarding the patient entirely. Therefore, for a given patient, one or more of the three available acquisitions, either in the long-axis or short-axis view, may have been omitted from the analysis, while the remaining valid frames were retained and used. Remaining missing values were imputed using k-Nearest Neighbors (KNN) imputation with $k = 5$, which allowed the method to leverage multivariate relationships among features for more accurate estimation. After preprocessing and feature selection, the final dataset consisted of 33 patients and 21 features (columns), to which the target class column (volemic status: hypovolemic, euvoletic, hypervolemic) was added, resulting in a 33×22 data matrix.

Clinical Features
Age
Sex
Plasma osmolality (mOsm/kg)
Spot urine sodium (mEq/L)
Urine osmolality (mOsm/kg)
ACTH (pg/mL)
Cortisol (nmol/L)
TSH (μ UI/mL)
FT4 (pg/mL)
Renin (μ UI/mL)
Aldosterone (ng/dL)
NT-proBNP (pg/mL)
Edema
Central venous pressure (CVP)

Table 4.2: Clinical features included in the initial dataset.

VIPER Derived Features
Max diameter (long-axis)
Min diameter (long-axis)
Mean diameter (long-axis)
Min diameter (short-axis)
Max diameter (short-axis)
Mean diameter (short-axis)
CI (long-axis)
RCI (long-axis)
CCI (long-axis)
CI (short-axis)
RCI (short-axis)
CCI (short-axis)

Table 4.3: Ultrasound features extracted using VIPER software.

4.4 Colab Environment and Python Frameworks

All analysis in this thesis were conducted using the Python programming language, taking advantage of its extensive ecosystem of data science libraries. The computational environment was based on Google Colab, which provides a cloud-based platform with access to GPUs and a pre-configured Python environment suitable for machine learning and statistical analysis.

4.4.1 Analysis of Repeatability

As previously mentioned, three acquisitions were collected for both the longitudinal-axis (LA) and short-axis (SA) views of each patient to evaluate intra-operator variability. These repeated measurements were specifically designed to evaluate intra-operator variability and the overall consistency of the measurement process using the VIPER software. Among the 33 patients enrolled in the study, only those with all six ultrasound videos available (three longitudinal and three transverse views) were included in this repeatability analysis. This criterion led to the inclusion of 24 subjects. Repeatability was comprehensively assessed using two complementary metrics: the Coefficient of Variation (CoV) and the Intraclass Correlation Coefficient (ICC).

ICC is a widely accepted metric for evaluating the reliability of quantitative measurements. The ICC quantifies the proportion of total variance attributable to differences between subjects, and is defined as follows:

$$\text{ICC} = \frac{\text{var}(S)}{\text{var}(S) + \text{var}(M) + \text{var}(E)} \quad (4.2)$$

where $\text{var}(S)$ represents the variance due to differences between subjects, $\text{var}(M)$ refers to the variance associated with different measurement sessions (i.e., intra-operator variability), and $\text{var}(E)$ denotes the residual error variance. A higher ICC value indicates greater repeatability and lower intra-operator variability.

The Intraclass Correlation Coefficient was calculated using a two-way random effects model for single measures, commonly referred to as ICC(2,1). This model is suitable in case the operators performs repeated acquisitions on the same subject. The two-way model accounts for variability both between subjects and between repeated measurements. This ICC model quantify the degree of consistency among repeated measures, reflecting the intra-operator repeatability. High ICC values indicate strong agreement among repeated measures. The 95% Confidence Interval (CI95%) for the ICC was also computed, providing a range within which the true ICC value is expected to fall with 95% certainty. A narrower CI95% indicates a more precise estimate of the ICC. The ICC calculations also yield an F-statistic from the associated Analysis of Variance (ANOVA). This F-statistic tests the null hypothesis that there are no true differences between subjects (i.e., the variance between subjects is negligible compared to the measurement error). A large F-statistic, along with its corresponding p-value (the probability of observing such a statistic under the null hypothesis), indicates that the differences between subjects are statistically significant. For repeatability analysis, a very low p-value ($p < 0.05$) is desirable as it confirms that the measurement system can consistently capture actual differences between subjects. The ICC calculations were performed using the `intraclass_corr` function from the `pingouin` Python library (version 0.5.5).

In addition to ICC, the Coefficient of Variation (CoV) was calculated for each parameter. The CoV represents the ratio between the standard deviation and the mean of repeated measurements acquired for each subject. It quantifies the relative variability of a parameter across different acquisitions performed by the same operator. To assess overall intra-operator repeatability, the mean CoV is then computed across all subjects for each parameter.

4.4.2 Analysis of Group Differences and Feature Ranking for Group Discrimination

To identify the most discriminating variables among the groups (hypo-, eu-, hyper-volemic) and to assess the statistical significance of these differences, two complementary statistical tests were employed based on variable type: the Kruskal-Wallis test for continuous variables and Fisher's exact test for binary categorical variables. The objective was to gain a comprehensive understanding of which parameters are most informative for classifying volemic status.

Normality Assessment of Variables

Before conducting a statistical analysis, the Shapiro-Wilk test was used to assess the normality of the distribution of each variable within each of the three groups

(hypovolemic, euvoletic and hypervolemic). This step wanted to analyse whether the data within each group followed a normal distribution. The results of this analysis guided the choice of the most appropriate statistical methods.

Analysis of Statistical Significance for Continuous Variables: Kruskal-Wallis Test

The Kruskal-Wallis test is a non-parametric method, which does not require the assumption of normality and it is robust to outliers. This test evaluates the null hypothesis that the medians of the groups are equal. The aim was to assess the presence of significant differences in the distributions of continuous variables across the three volentic groups. A p-value below 0.05 was considered indicative of a statistically significant difference among at least two of the three groups. In addition, the Kruskal-Wallis H-statistic was used in order to provide a metric for a preliminary ranking of features according to their discriminatory power among the groups.

Analysis of Statistical Significance for Binary Variables: Fisher’s Exact Test

Fisher’s Exact test was used for binary categorical variables, in order to evaluate differences in the distribution across the three volentic groups. Fisher’s Exact Test is a statistical test used to evaluate the association between two categorical variables arranged in a contingency table, such as a 2x3 table. It calculates the probability of obtaining the observed contingency table under the null hypothesis of independence between categorical variables, on the condition of fixed marginal totals (i.e., the row and column sums). It evaluates all the possible tables consistent with these margins and then sums the probabilities of those with configurations more extreme than the observed table, producing a p-value. This approach is appropriate for small sample sizes or sparse data. Variables with p-values below 0.05 were considered to show statistically significant differences between groups.

4.4.3 Analysis of ML models for classification

The objective of this study was to evaluate whether the addition of ultrasound-derived features, extracted via the VIPER software tool, to standard clinical variables could enhance the classification of hyponatremic patients into three volentic categories: hypovolemic, euvoletic, and hypervolemic. The secondary aim was to identify a minimal subset of features capable of achieving reliable classification performance.

Three classification models were initially explored to assess their predictive performance on clinical variables only and then on the complete dataset:

- Logistic Regression
- Linear Support Vector Machine Classifier (Linear SVC)

- Random Forest (RF) Classifier

Each model was optimized using grid search for hyperparameter tuning, and performance was assessed using balanced accuracy and weighted F1-score, in order to account for the imbalance among the three classes (6 hypovolemic, 14 euvolemic, and 13 hypervolemic patients). Both Linear SVC and Random Forest produced comparable and superior results compared to Logistic Regression, and were therefore retained for subsequent analyses.

A 3-fold stratified cross-validation was applied, in order to ensure robust model evaluation, despite the limited sample size and class imbalance. In this way class proportions within each fold was maintained. The most relevant features, for each fold, were identified using the `SelectFromModel` method, with the selection threshold set to the mean feature importance. For the Linear SVC (with L1 regularization), feature selection was based on the magnitude of model coefficients [38], whereas for the Random Forest model, feature importance was computed using the Mean Decrease in Impurity (MDI) criterion [6, 16]. Each model identified a different subset of features as most relevant for the classification task. These subsets were evaluated in terms of average contribution to model performance and stability across folds, by computing a weighted frequency score indicating how often each feature was selected. This process enabled the derivation of two independent global rankings of feature importance, one for each model. A grid search was conducted to identify the most effective combinations of a reduced set of features. In order to isolate the added value of VIPER-derived features, the number of clinical variables included in the grid search was intentionally restricted. Only the most informative clinical features, *CVP* and *Edema*, and all VIPER-derived ultrasound features (both in long and short-axis view) were retained. All possible subsets of these variables (with at least one feature) were evaluated with performance assessed using the same stratified cross-validation protocol and evaluation metrics. The Random Forest model consistently outperformed Linear SVC during this reduced feature selection phase. Consequently, the best-performing feature subset obtained with Random Forest was further evaluated using a leave-one-out cross-validation (leaving out one patient per fold), to reduce the bias in error estimation, considering the limited dataset.

Importance coefficients in Random Forest Classifier

In Random Forest classifiers, feature importance is computed using the *Mean Decrease in Impurity* (MDI), as implemented in `scikit-learn`'s `RandomForestClassifier` via the `feature_importances_` attribute. This method assesses the contribution of each feature to the model by measuring how much it reduces the impurity (e.g., Gini impurity) at each split in the decision trees. Every time a feature is used to split a node, the associated decrease in impurity is recorded. The overall importance score for each feature is then obtained by averaging these impurity reductions across all trees in the forest.

This metric allows to capture non-linear relationships and feature interactions, but it is known to be biased toward features with high cardinality.

Importance coefficients in Linear Support Vector Machine Classifier

For the Linear Support Vector Machine Classifier (`LinearSVC`), the importance of a feature is derived from the model’s learned coefficients, accessible through the `coef_` attribute. The classifier optimizes a linear decision function defined as:

$$f(\mathbf{x}) = \mathbf{w}^\top \mathbf{x} + b, \quad (4.3)$$

where \mathbf{w} is the weight vector, and each coefficient w_j reflects the direction and magnitude of the feature contribution x_j to the decision boundary. The larger the absolute value of w_j , the more influence the corresponding feature has on the classification decision. These coefficients are determined by solving an optimization problem that balances misclassification penalty and margin maximization, using the regularization parameter C [38]. Unlike tree-based models, Linear SVC assumes a linear relationship between input features and the output class.

Chapter 5

Results

5.1 Repeatability Analysis Results

The repeatability analysis yielded comprehensive insights into the consistency of IVC measurements, with results summarized in Table 5.1 (ICC values) and Table 5.2 (MSD values).

View	Feature	ICC	CI95%	F	p-value
SA	Mean Diameter	0.97	[0.94, 0.98]	85.84	2.15e-30
SA	CI	0.87	[0.76, 0.93]	19.88	7.92e-17
SA	RCI	0.92	[0.86, 0.96]	35.86	4.02e-22
SA	CCI	0.90	[0.82, 0.95]	28.05	7.03e-20
LA	Mean Diameter	0.89	[0.79, 0.94]	23.75	2.19e-18
LA	CI	0.62	[0.4, 0.79]	5.91	1.66e-07
LA	RCI	0.75	[0.58, 0.87]	9.69	5.76e-11
LA	CCI	0.83	[0.7, 0.92]	17.63	8.57e-16

Table 5.1: Intraclass Correlation Coefficient (ICC) Results for Repeatability.

View	Feature	Mean CoV (%)
SA	Mean Diameter	3.6
SA	CI	17.1
SA	RCI	24.0
SA	CCI	16.6
LA	Mean Diameter	8.6
LA	CI	28.3
LA	RCI	34.4
LA	CCI	21.3

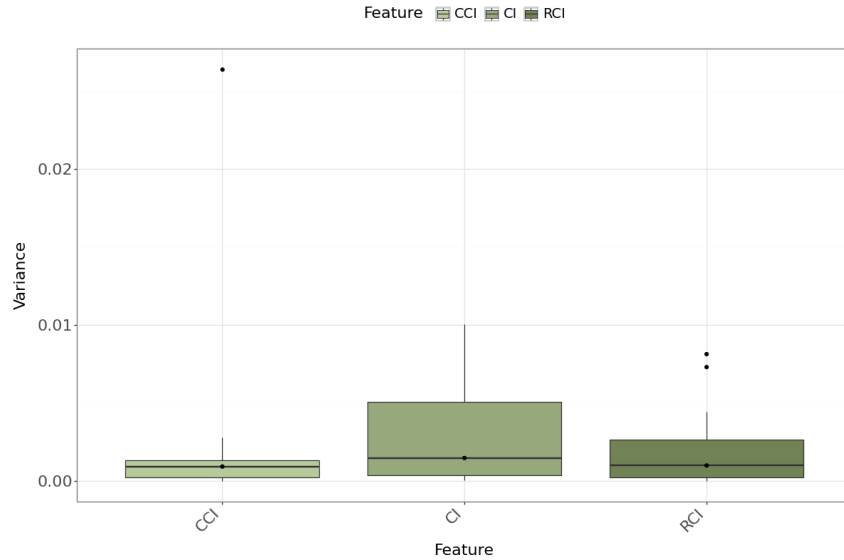
Table 5.2: Mean Coefficient of Variation (CoV) for Intra-Operator Variability.

The repeatability analysis of ultrasound IVC measurements showed high consistency for short-axis parameters, with ICC values above 0.90 for mean diameter,

RCI, and CCI, and CoV values indicating low variability across all measurements. In contrast, long-axis parameters exhibited lower repeatability, especially for CI (ICC = 0.62), accompanied by higher intra-subject variability as reflected by increased coefficients of variation (CoV) (Table 5.2). For all measurements, the ICC values were accompanied by F-test results, which assess the ratio of inter-subject to intra-subject variability. Although F-test values were consistently lower for LA measurements compared to SA, reflecting relatively higher intra-subject variability in the LA view, all tests yielded statistically significant p-values ($p < 0.001$). This confirms that, despite the increased intra-subject variability in LA, the variability between subjects remains significantly greater than within subjects, supporting the reliability of the measurements.

Given the the ICC of 0.62 of the *LA / CI* feature, a closer inspection of intra-subject variance has been made, especially for the collapsibility indices (Figures 5.1, 5.2). The analysis revealed that a small number of subjects exhibited higher values of variance intra-subject in the LA view, especially for CI. Two subjects in particular, subject 22 and subject 9 showed frames in which the IVC was not clearly visible due to partial disappearance in certain video segments, likely caused by bowel gas. In such cases, the segmentation algorithm may erroneously measure tissue outside the actual vessel, introducing random fluctuations across acquisitions.

Figure 5.3 illustrates this phenomenon for subject 22, where the IVC is not consistently visible across frames, leading to high intra-subject variability in collapsibility measurements. These outlier cases are also visible in the boxplot of intra-subject variances (Figures 5.1, 5.2), with the majority occurring in the longitudinal view.



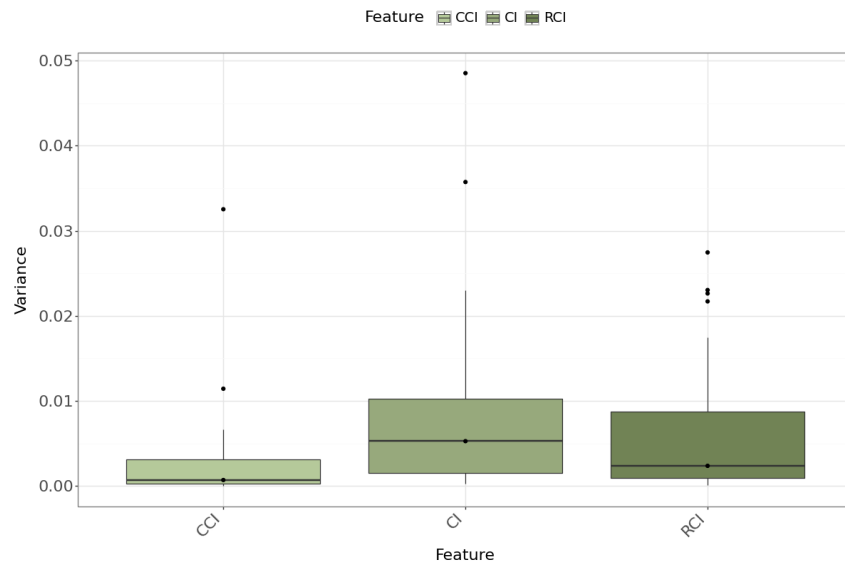
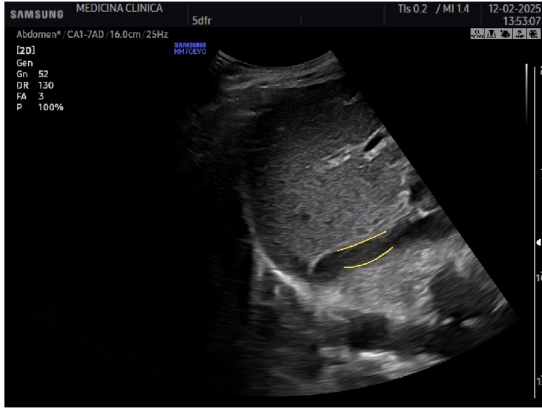


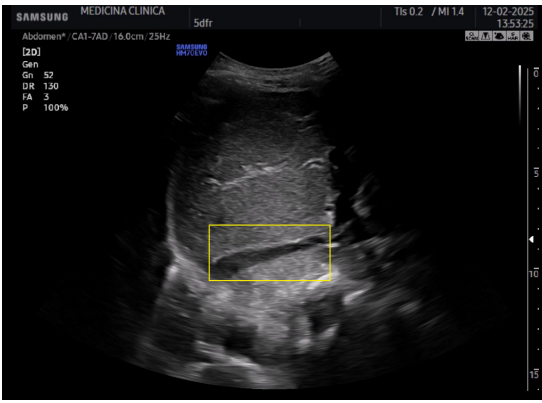
Figure 5.2: Boxplot showing the distribution of intra-subject variance (over three acquisitions) across patients for LA collapsibility indices.



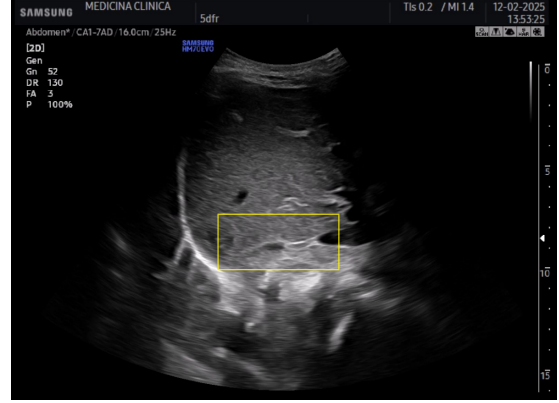
(a) Video 1 – frame A



(b) Video 1 – frame B



(c) Video 2 – frame A



(d) Video 2 – frame B

Figure 5.3: Example frames from two long-axis acquisition videos for subject 22. In both videos the inferior vena cava (highlighted by the yellow rectangles) disappears partially or completely in some frames. This loss of visualisation forces the semi-automatic algorithm to segment a region that does not correspond to the actual vessel, leading to inconsistent measurement estimates and high intra-subject variability in the collapsibility indices.

5.2 Results of Group Comparison and Feature Ranking Analysis

Table 5.3 presents the results of the Shapiro-Wilk normality test for each variable within the three volemic groups (hypo-, eu-, hypervolemic). These results informed the selection of appropriate statistical tests for subsequent group comparisons by indicating whether the distribution of each variable within each group deviated from normality.

Variable	Class 0 (Hypo)	Class 1 (Eu)	Class 2 (Hyper)
Cortisol (nmol/L)	Normal	Normal	Not Normal
Edema	Normal	Not Normal	Not Normal
CVP	Normal	Not Normal	Not Normal
Age	Not Normal	Not Normal	Not Normal
Sex	Normal	Not Normal	Not Normal
NT-proBNP (pg/mL)	Normal	Not Normal	Not Normal
Plasma Osmolality (mOsm/kg)	Normal	Normal	Not Normal
TSH (μ IU/mL)	Normal	Not Normal	Normal
FT4 (pg/mL)	Normal	Normal	Normal
LA / CCI	Normal	Not Normal	Not Normal
LA / CI	Not Normal	Normal	Normal
LA / Max Diameter	Normal	Normal	Normal
LA / Mean Diameter	Normal	Normal	Normal
LA / Min Diameter	Normal	Normal	Normal
LA / RCI	Not Normal	Normal	Not Normal
SA / CCI	Not Normal	Not Normal	Not Normal
SA / CI	Not Normal	Normal	Not Normal
SA / Max Diameter	Normal	Normal	Normal
SA / Mean Diameter	Normal	Normal	Normal
SA / Min Diameter	Normal	Normal	Normal
SA / RCI	Not Normal	Normal	Not Normal

Table 5.3: Shapiro-Wilk normality test results for each variable across the three diagnostic classes.

The results assessing the differences across the three volemic status groups are summarized in Table 5.4. Table 5.5 reports all continuous features sorted by decreasing H-statistic, providing a useful ranking of their ability to discriminate between the three volemic status groups. Several features showed statistically significant differences across groups. In particular, NT-proBNP ($p = 0.01$), Plasma Osmolality ($p = 0.05$) and LA Min Diameter ($p = 0.05$) reached conventional significance ($p < 0.05$). Among the binary categorical variables, both Edema ($p = 0.0001$) and CVP ($p = 0.0006$) showed statistically significant differences in their distribution across the three volemic groups, as assessed by the Fisher exact test. Frequency bar plots for these binary features are presented in Figure 5.6, highlighting the distribution of Edema (0 = absent, 1 = present), CVP (0 = normal, 1 = elevated), and Sex (0 = female, 1 = male) across the volume status categories. To better visualize the differences observed in continuous variables, boxplots were generated for the numerical features tested with Kruskal-Wallis (Figure 5.4, Figure 5.5), ordered by descending H-statistic.

Feature	Statistical Test	p-value
Edema	Fisher exact test	0.0001
CVP	Fisher exact test	0.0006
NT-proBNP (pg/mL)	Kruskal-Wallis	0.01
Plasma Osmolality (mOsm/kg)	Kruskal-Wallis	0.05
LA / Min Diameter	Kruskal-Wallis	0.05
SA / Max Diameter	Kruskal-Wallis	0.07
Sex	Fisher exact test	0.08
SA / Mean Diameter	Kruskal-Wallis	0.08
LA / Mean Diameter	Kruskal-Wallis	0.09
LA / Max Diameter	Kruskal-Wallis	0.11
Cortisol (nmol/L)	Kruskal-Wallis	0.14
FT4 (pg/mL)	Kruskal-Wallis	0.22
SA / RCI	Kruskal-Wallis	0.31
LA / CCI	Kruskal-Wallis	0.32
SA / Min Diameter	Kruskal-Wallis	0.36
LA / RCI	Kruskal-Wallis	0.38
LA / CI	Kruskal-Wallis	0.45
SA / CI	Kruskal-Wallis	0.62
TSH (μ IU/mL)	Kruskal-Wallis	0.64
SA / CCI	Kruskal-Wallis	0.66
Age	Kruskal-Wallis	0.66

Table 5.4: Statistical test results for all features. Fisher’s exact test was used for categorical variables, and Kruskal-Wallis test for continuous ones. Statistically significant p-values ($p \leq 0.05$) are highlighted in bold.

Feature	Kruskal-Wallis H	p-value
NT-proBNP (pg/mL)	9.18	0.01
Plasma Osmolality (mOsm/kg)	6.16	0.05
LA / Min Diameter	5.93	0.05
SA / Max Diameter	5.44	0.07
SA / Mean Diameter	5.11	0.08
LA / Mean Diameter	4.76	0.09
LA / Max Diameter	4.44	0.11
Cortisol (nmol/L)	3.96	0.14
FT4 (pg/mL)	3.06	0.22
SA / RCI	2.37	0.31
LA / CCI	2.30	0.32
SA / Min Diameter	2.07	0.36
LA / RCI	1.95	0.38
LA / CI	1.61	0.45
SA / CI	0.97	0.62
TSH (μ IU/mL)	0.88	0.64
SA / CCI	0.84	0.66
Age	0.82	0.66

Table 5.5: Ranking of continuous features analyzed with the Kruskal-Wallis test, sorted by ascending p-value.

In Figure 5.4, the distributions of clinical features across the different volemic states are presented. The variables NT-proBNP and Plasma Osmolality exhibit a clear separation in the median values for the hypervolemic group compared to the hypovolemic and euvolemic groups.

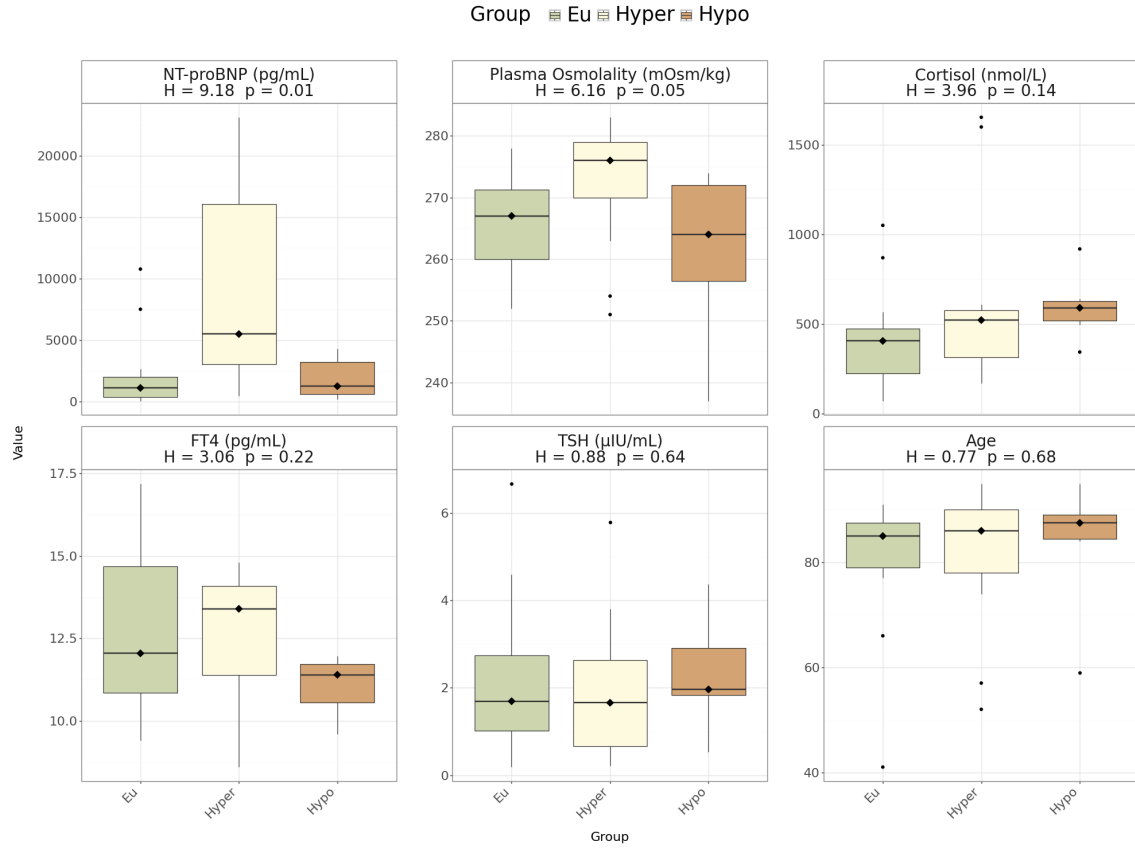


Figure 5.4: Distribution of the clinical features from patients with different volemic condition (hypo-, eu-, hypervolemic). The plots visualize inter-group separation and within-group variability.

In Figure 5.5, the distributions of the VIPER-extracted echocardiographic features, derived from both the long and short axes, are displayed across the three volemic states. Among these, LA / Min Diameter, SA / Max Diameter, SA / Mean Diameter, and LA / Mean Diameter show modest differences in median values across the groups. In contrast, the remaining variables do not exhibit appreciable differences in their median distributions.

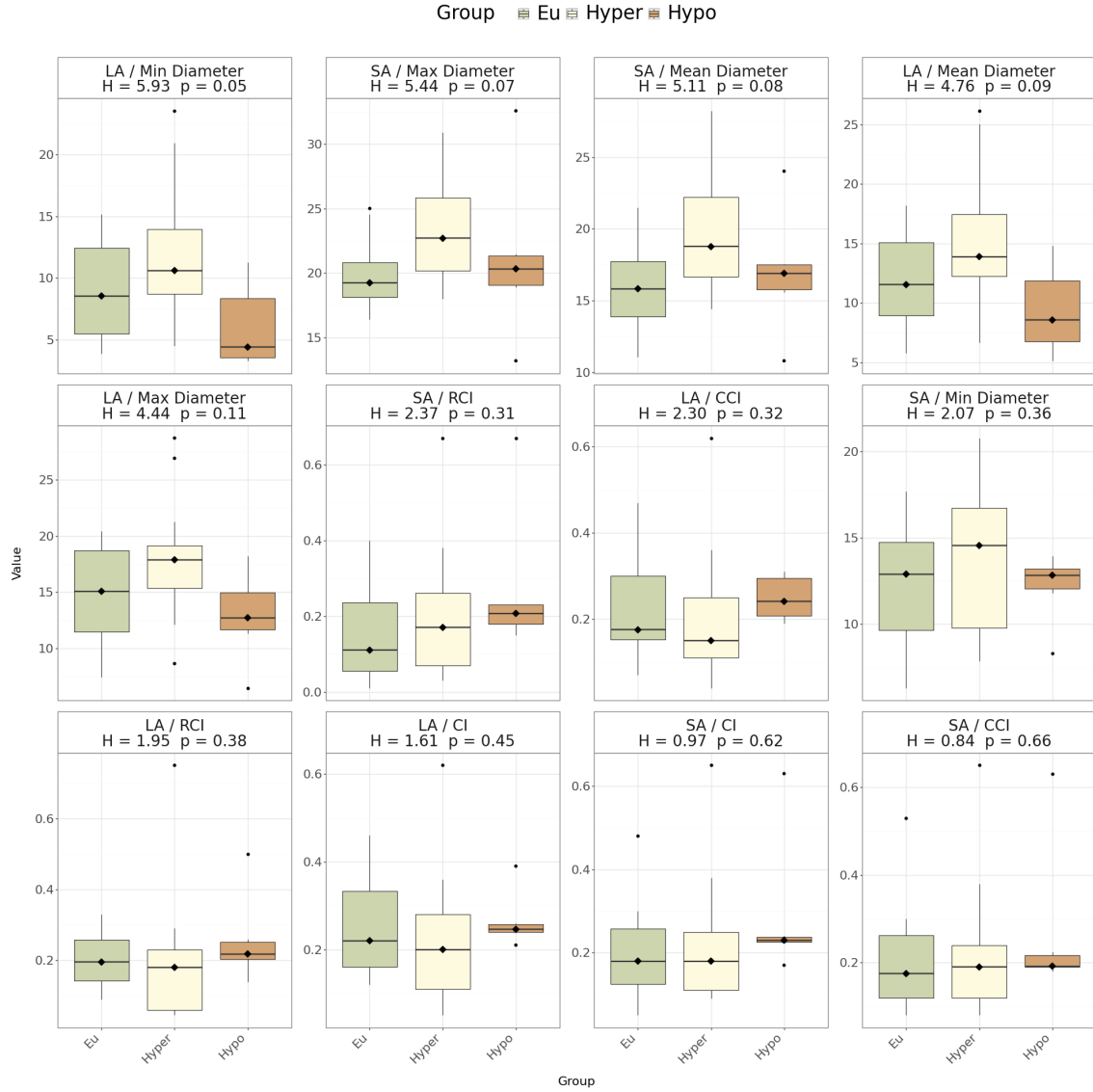


Figure 5.5: Distribution of VIPER-derived features across patients with different volemic conditions (hypo-, eu-, and hypervolemic). Group differences were evaluated using the Kruskal–Wallis test; H denotes the test statistic, and the associated p -value (from the chi-squared distribution) indicates the likelihood of observing such differences by chance. A p -value < 0.05 denotes statistically significant inter-group variation. The plots illustrate both inter-group separation and intra-group variability.

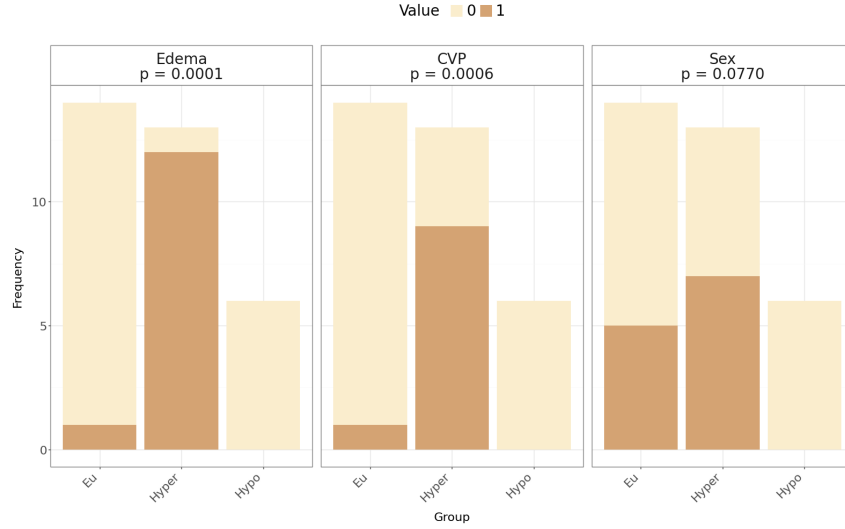


Figure 5.6: Bar plots showing the absolute frequencies of patients across volume status groups (hypo-, eu-, hypervolemic) for the binary features analyzed using Fisher’s exact test. Feature codings are as follows: Edema (0 = absent, 1 = present), CVP (0 = normal, 1 = elevated), and Sex (0 = female, 1 = male). The y-axis represents the number of patients in each category within the corresponding group.

As shown in Figure 5.6, Edema and CVP display a higher frequency of value 1 in the hypervolemic group, indicating a greater prevalence of these conditions in this group.

5.3 Results of ML models analysis

All three classifiers showed improved performance when VIPER features were added to the clinical variables, as shown in Table 5.6, Table 5.7 and Table 5.8. The inclusion of VIPER features led to an increase in both balanced accuracy and weighted F1-weighted score across models.

Feature Set	Balanced Accuracy	F1-score (weighted)
Clinical only	0.572	0.520
Clinical + VIPER	0.633	0.635

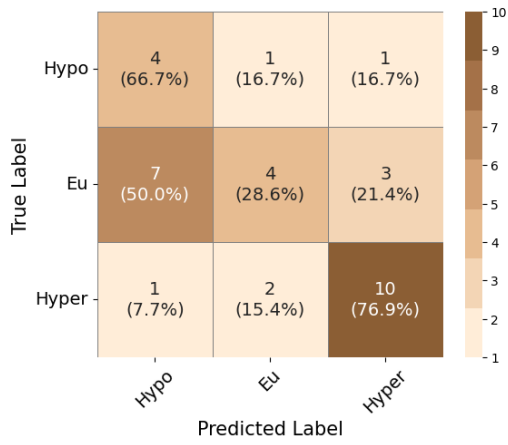
Table 5.6: Performance of Logistic Regression classifier.

Feature Set	Balanced Accuracy	F1-score (weighted)
Clinical only	0.572	0.528
Clinical + VIPER	0.750	0.703

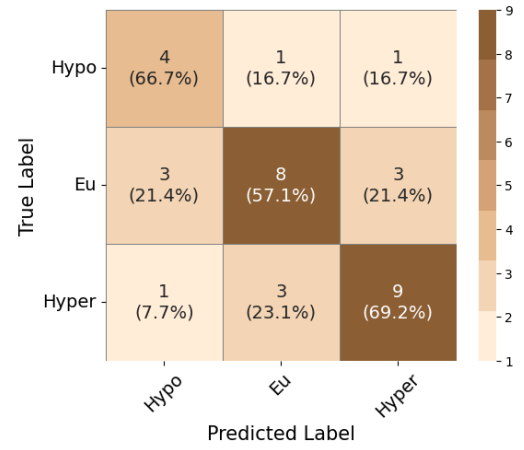
Table 5.7: Performance of Linear SVC.

Feature Set	Balanced Accuracy	F1-score (weighted)
Clinical only	0.678	0.636
Clinical + VIPER	0.717	0.729

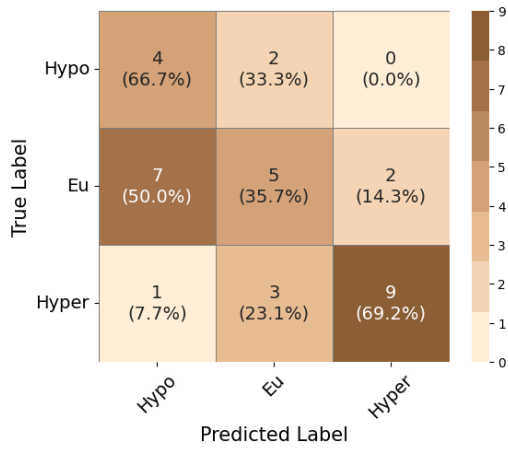
Table 5.8: Performance of RF classifier.



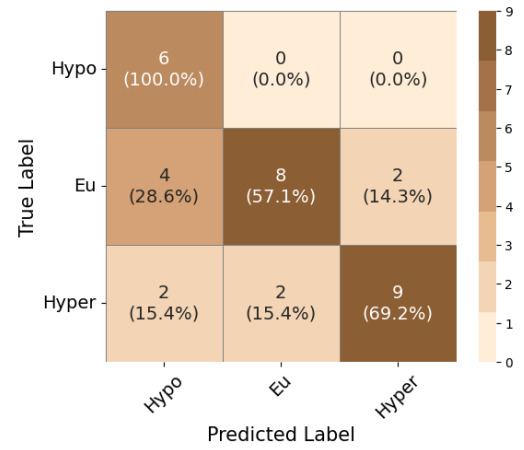
(a) Logistic Regression - clinical



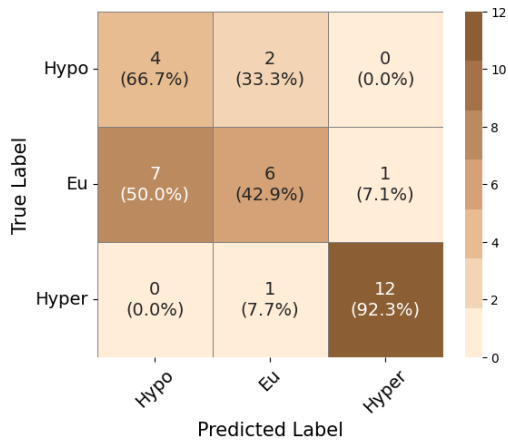
(b) Logistic Regression - clinical + viper



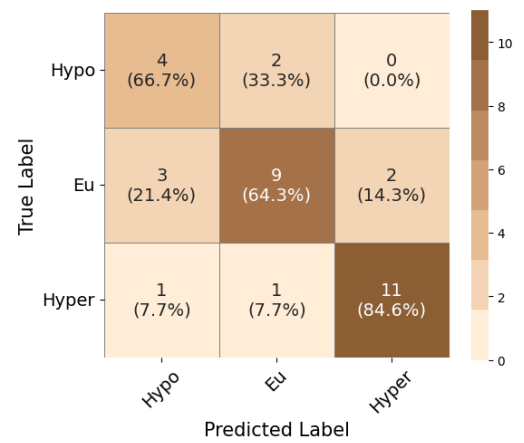
(c) Linear SVM - clinical



(d) Linear SVM - clinical + viper



(e) RF - clinical



(f) RF - clinical + viper

Figure 5.7: Confusion matrices for different classifiers using only clinical and clinical + viper variables.

Among the three classifiers, Linear SVM and RF classifiers achieved comparable overall results. Tables 5.9 and 5.10 report the features selected by the Linear Support Vector Machine and Random Forest classifiers, respectively. For each feature, both the average importance score and its selection weight (i.e., the number of folds in which it was selected, normalized to the total number of folds) are reported. This provides insight into both the relative influence and stability of each feature across cross-validation folds.

Feature	Coefficient Importance	Selection Weight
NT-proBNP (pg/mL)	0.124	0.333
SA / Min Diameter	0.107	0.333
LA / CI	0.105	0.333
FT4 (pg/mL)	0.061	0.667
SA / RCI	0.047	0.667
LA / Min Diameter	0.039	0.667
LA / RCI	0.018	0.333
Plasma Osmolality (mOsm/kg)	0.011	0.333
Cortisol (nmol/L)	0.006	0.333
LA / CCI	-0.009	0.333
Edema	-0.057	1.000
CVP	-0.137	0.333
SA / CCI	-0.168	0.667
Sex	-0.217	0.667
SA / Mean Diameter	-0.314	0.333

Table 5.9: Linear SVC selected features ordered by average importance. Both the coefficient importance and the mean selection weight across folds are reported.

Feature	Coefficient Importance	Selection Weight
Edema	0.216	1.000
CVP	0.087	0.333
TSH (μ IU/mL)	0.069	0.667
LA / Min Diameter	0.065	0.667
LA / CCI	0.061	1.000
SA / CI	0.060	0.333
NT-proBNP (pg/mL)	0.056	1.000
SA / Max Diameter	0.053	0.333
SA / RCI	0.051	0.667
SA / Mean Diameter	0.041	0.333
FT4 (pg/mL)	0.040	0.333
LA / Mean Diameter	0.025	0.333
Sex	0.019	0.333
Cortisol (nmol/L)	0.017	0.333

Table 5.10: RF selected features ordered by average importance. Both the coefficient importance and the mean selection weight across folds are reported.

Figures 5.8 and 5.9 show bar plots of the selected features for the Linear SVM and Random Forest classifiers. The length of each bar represents the product between the feature's importance score and its selection weight, effectively combining both magnitude and consistency of selection.

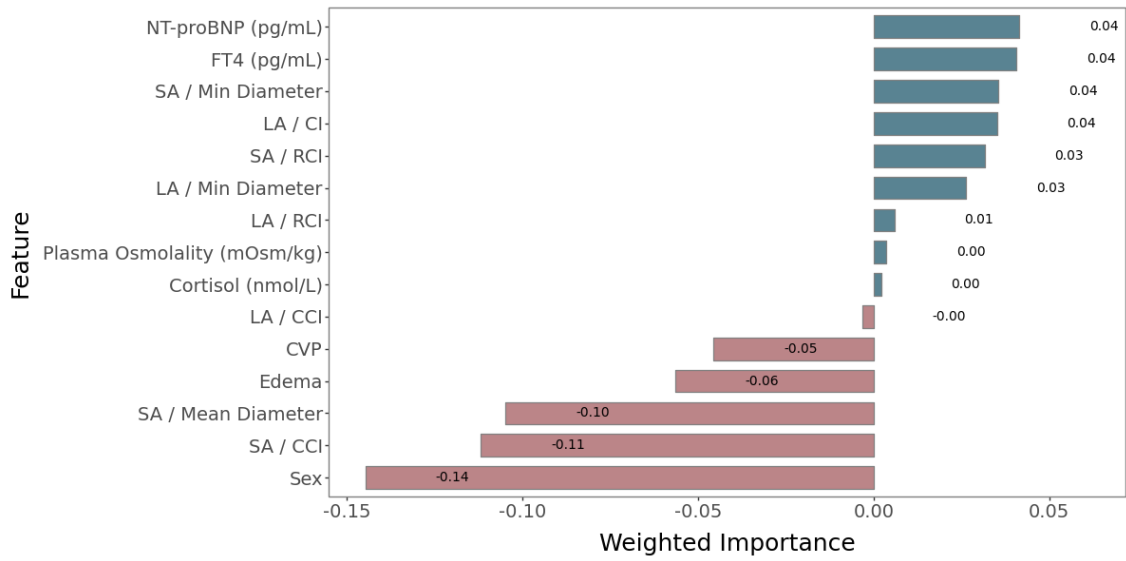


Figure 5.8: Global ranking of weighted importance of the features selected by the Linear SVM model. The length of each bar is given by the product of the coefficient value and the selection frequency across folds. Bar colors indicate the sign of the coefficient: blue for positive and red for negative associations with the target variable. While the sign reflects the direction of the effect, the importance is determined by the absolute value of the coefficient, which reflects the strength of the contribution.

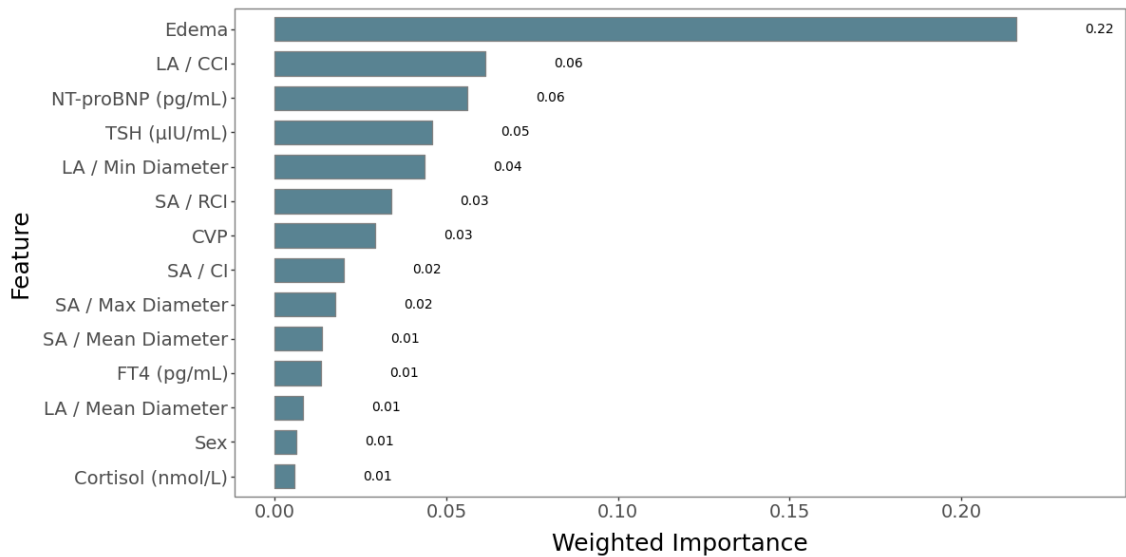


Figure 5.9: Global ranking of weighted importance of the features selected by the RF model. The bar length corresponds to the coefficient importance multiplied by the selection weight across folds.

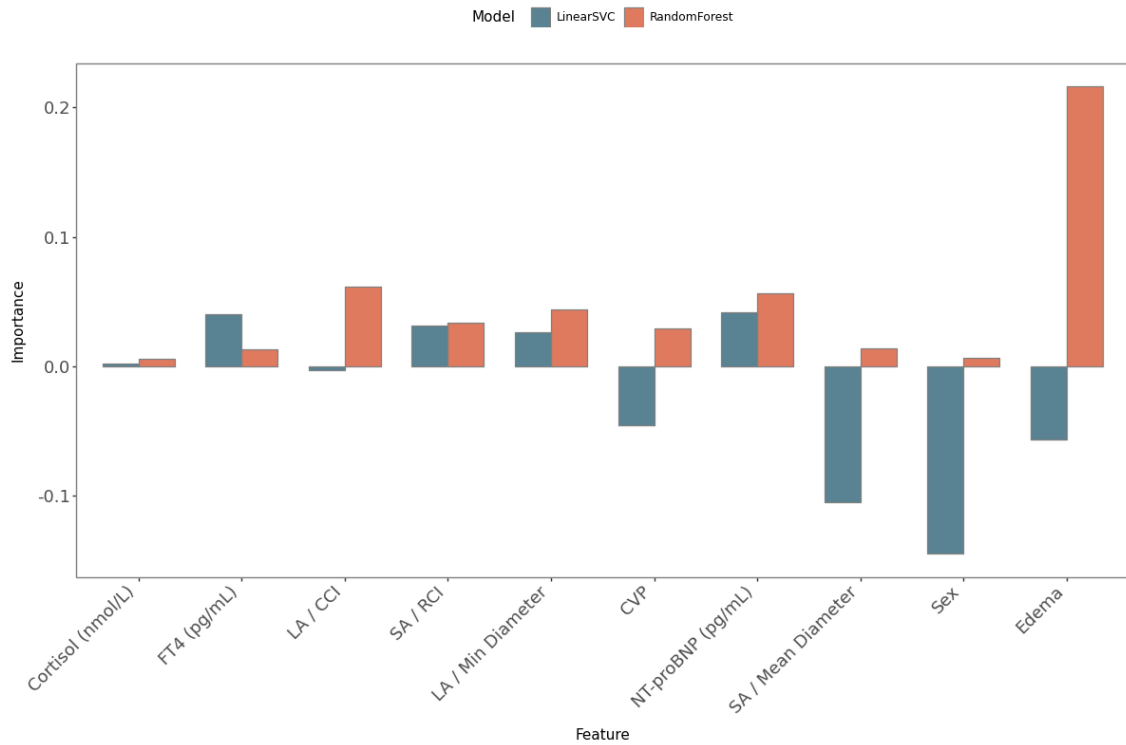


Figure 5.10: Common features selected by both Linear SVM and Random forest classifiers.

Figures 5.11 and 5.12 show the results of PCA and t-SNE analyses performed on the features selected by the Linear SVM model. In the PCA projection, there is not a clear pattern or separation between classes. The t-SNE projection shows a pattern in the distribution, but the selected feature set is still not able to form defined clusters.

A similar tendency can be observed in Figures 5.13 and 5.14, which show the PCA and t-SNE analyses performed on the features selected by the Random Forest classifier. As with the features selected by Linear SVM, the PCA projection does not show any clear class separation, while the t-SNE projection suggests a more organized distribution, but without forming separate clusters.

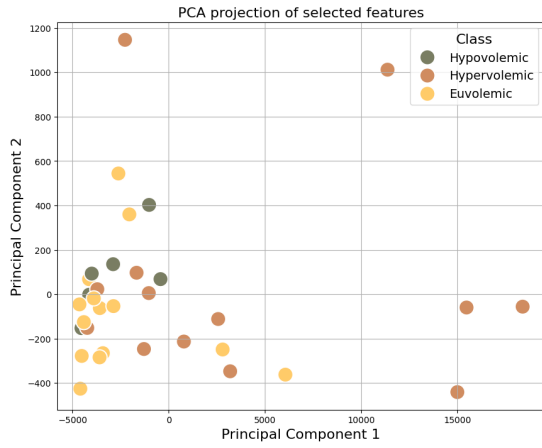


Figure 5.11: PCA of the features selected by Linear SVC.

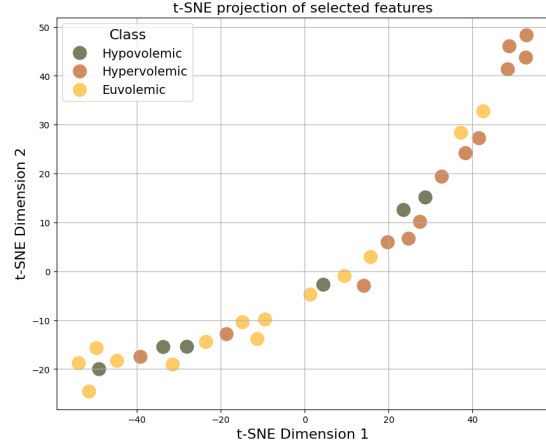


Figure 5.12: tSNE of the features selected by Linear SVC.

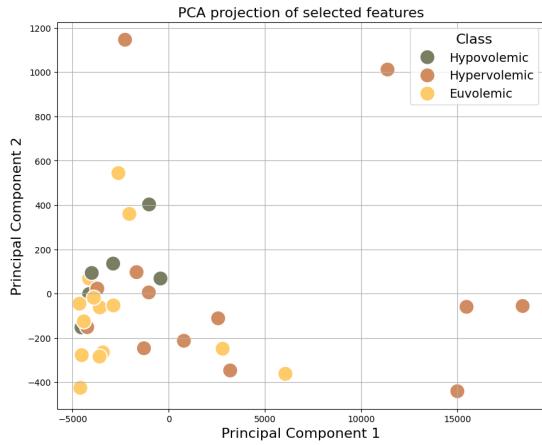


Figure 5.13: PCA of the features selected by Random Forest classifier.

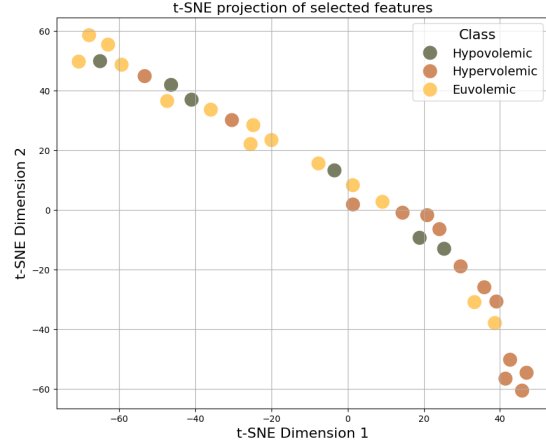


Figure 5.14: tSNE of the features selected by Random Forest classifier.

The results of the grid search conducted using both models are shown in Tables 5.11 and 5.13. The Random Forest classifier achieved higher performance compared to the Linear SVC, using a minimal subset of features. Based on these results, the Random Forest model with its selected feature set was chosen as the final classifier.

Feature Subset (Linear SVC)	Balanced Accuracy	Weighted F1-score
Edema, SA / Max Diameter, SA / Min Diameter, SA / RCI, LA / Mean Diameter, LA / RCI	0.899	0.886

Table 5.11: Best-performing feature subset for Linear SVC selected via grid search.

Feature Subset (Random Forest)	Balanced Accuracy	Weighted F1-score
Edema, SA / Max Diameter, SA / CCI, LA / CCI	0.908	0.889

Table 5.12: Best-performing feature subset for Random Forest selected via grid search.

Figures 5.15 and 5.16 show the PCA and t-SNE visualizations obtained using the best performing subset of features, selected through grid search optimization. Compared to the previous feature sets, the resulting plots now show more evident clustering patterns, although there is still not a clear separation between classes.

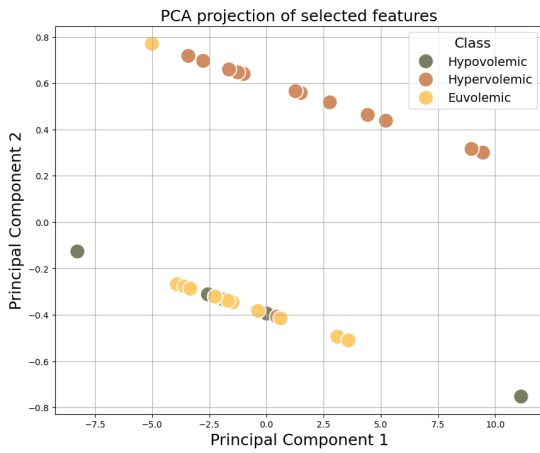


Figure 5.15: PCA with the features selected by the grid search.

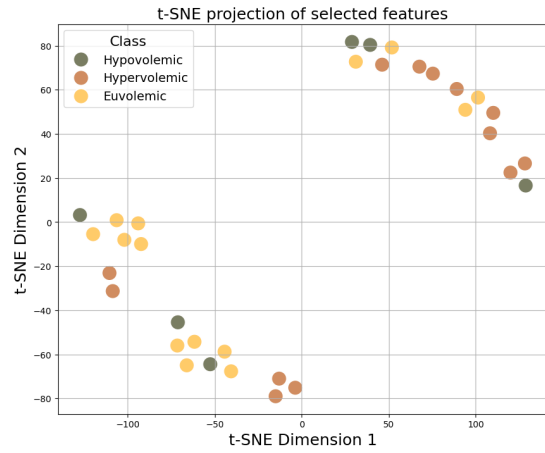


Figure 5.16: tSNE with the features selected by the grid search.

To obtain an unbiased performance estimate on the small dataset, the final model (Random Forest) was evaluated using Leave-One-Out Cross-Validation (LOOCV), trained and tested on the optimal subset of features previously selected via Grid Search. The corresponding results are reported in Table 5.13.

Feature Subset (Random Forest)	Balanced Accuracy	Weighted F1-score
Edema, SA / Max Diameter, SA / CCI, LA / CCI	0.818	0.818

Table 5.13: Performance of the final model evaluated through leave-one-out cross-validation on the optimal subset of features.

Chapter 6

Discussion of the Results

6.1 Statistical significances between groups

The statistical analysis revealed that four clinical features, Edema, Central Venous Pressure (CVP), NT-proBNP, and Plasma Osmolality, showed significant differences between at least two of the three groups considered. As illustrated in Figure 5.4, NT-proBNP and Plasma Osmolality show a clear separation in median values between the hypervolemic group and the other two groups. As shown in Figure 5.6 both Edema and CVP display a higher frequency of value 1 for the hypervolemic group, which indicate a greater prevalence of these conditions in the hypervolemic population. This suggests that these features may have some discriminative power in identifying hypervolemic patients compared to the hypovolemic and euvolemic groups. These findings are consistent with existing literature. Peripheral edema is a classical clinical sign of fluid overload and is strongly associated with hypervolemic hyponatremia [9]. Similarly, elevated CVP reflects increased right atrial pressure and is frequently used as an indirect marker of intravascular volume status. As said in Section 1.1.4, it has been widely adopted in critical care to assess fluid responsiveness and overload, despite its numerous limitations. Among the VIPER-derived features, those related to the inferior vena cava (IVC) diameters exhibited the lowest p-values in the Kruskal-Wallis analysis, suggesting a potential discriminatory role across the three volume status groups. In particular, Figure 5.5 shows that the feature *LA / Min Diameter* displays a clearly lower median value in the hypovolemic group compared to the euvolemic and hypervolemic groups. A similar pattern is observed for *LA / Mean Diameter*, supporting the relevance of IVC size in distinguishing hypovolemia. These findings are consistent with the physiological expectation that a collapsed IVC, manifesting as a reduced diameter, can reflect decreased venous return and circulating volume, as commonly seen in hypovolemic patients.

On the other hand, most of the collapsibility indices did not show statistically significant differences between groups ($p > 0.05$), indicating that static diameter measurements may provide greater discriminatory power than dynamic indices in this setting. However, this observation might also reflect the variability and technical

challenges of measuring IVC collapsibility in clinical practice.

The differences reported here are the result of univariate statistical tests. Each test examines a single feature in isolation, asking whether its distribution differs significantly across the three volume status groups. In other words, these tests measure the marginal discriminative power of one variable at a time. They do not capture potential interactions between features, nor non-linear relationships that might emerge only when variables are considered jointly.

6.2 Interpretation of Machine Learning Model Performance

6.2.1 Added Value of VIPER Features

As presented in Section 5.3, the performance of three different classifiers, Logistic Regression, Linear Support Vector Classifier, and Random Forest, was evaluated under two conditions: using only clinical variables and using both clinical and VIPER-derived features. In all cases, the inclusion of VIPER features resulted in improved classification performance.

The confusion matrices showed that the highest improvement was observed in the prediction of the euvolemic class. The addition of VIPER features allowed the classifiers to better discriminate between the euvolemic and hypovolemic states, which are traditionally more difficult to distinguish. On the other side, the hypervolemic class was already well identified using clinical features alone, which is consistent with existing clinical knowledge.

With the integration of VIPER variables, the proportion of correctly classified euvolemic cases increased markedly: from 28.6% to 57.1% for Logistic Regression (Figure 5.7a→5.7b), from 35.7% to 57.1% for Linear SVC (Figure 5.7c→5.7d), and from 42.9% to 64.3% for Random Forest (Figure 5.7e→5.7f). Notably, the Linear SVC model achieved perfect classification for the hypovolemic class, an encouraging outcome given the small sample size of this group and the known difficulty of identifying hypovolemia based on clinical parameters alone.

As reported in the literature, the hypervolemic class is generally easier to classify even with traditional clinical markers. This finding is confirmed in the present analysis: all classifiers reached high accuracy for this class using only clinical features (e.g., over 85% in all cases), with performance either remaining stable or slightly improving when VIPER features were included.

In summary, the addition of VIPER-derived features enhanced the classifiers' ability to distinguish not only the hypervolemic class, which was already well detected, but also the more ambiguous hypovolemic and, in particular, euvolemic classes. These results suggest that VIPER provides clinically relevant information and may contribute to more accurate assessment of volume status in hyponatremic patients, beyond what is achievable with routine clinical data alone.

6.2.2 Evaluation of the feature selection

The feature selection analysis performed on the two best-performing classifiers (Linear SVM and Random Forest) highlights both convergence and divergence in the predictive variables identified, depending on the nature of the model. Figures 5.8 and 5.9 illustrate the global ranking of features, obtained by combining the average importance with the selection frequency across cross-validation folds. This score captures not only how often a feature was selected, but also how strongly it contributed to the model’s predictions.

For the Linear SVM model, the global ranking shows that features with higher coefficients magnitude are *Sex*, *SA/CCI* and *SA/Mean Diameter*. They all have negative coefficients, indicating they contribute significantly to class separation but push the decision boundary in the opposite direction. *Edema* and *CVP* also play important roles, which is consistent with their clinical relevance and the findings of the univariate analysis. Other ultrasound features, such as *SA/RCI* and *LA/Min Diameter* have moderate selection weights, suggesting they add complementary linear information when combined with clinical variables.

For Random Forest, similar to the SVM, *Edema* remains the most important feature, but additional variables such as *LA/CCI*, *NT-proBNP* and *TSH* also show notable importance. This highlights the fact that variables that might not emerge as strongly in a linear model, may be more important for this model, which capture complex relations.

Although univariate analysis assigned greater discriminative importance to diameter related VIPER features, both models show that features related to both diameter and collapsibility contribute to classification. As illustrated in the Figure 5.10, which displays the features commonly selected by both models, these include VIPER features related to diameter and collapsibility indices, as well as two of the most discriminative clinical variables, *Edema* and *CVP*. Since the models capture different types of interactions, Linear SVM identifies linear relationships, while Random Forest (RF) captures more complex, non linear interactions, they select different feature sets. However, both consistently confirm the importance of VIPER features alongside clinical variables such as *Edema* and *CVP*. This suggests that while diameter measurements alone are important, incorporating collapsibility indices and clinical variables provide a richer picture of volume status classification.

To further investigate the discriminative power of the features selected by the two classifiers, dimensionality reduction techniques, Principal Component Analysis (PCA) and t-distributed Stochastic Neighbor Embedding (t-SNE), were applied. These analyses were conducted separately on the subsets of features identified by the Linear SVM and Random Forest models, in order to visualize how well the selected features can separate the target classes in lower-dimensional space, thereby capturing linear and non-linear structures, respectively. The PCA projections (Figures 5.11 and 5.13) did not show clear cluster separation for either classifier. The data points remain largely overlapping, with no evident boundaries between hypovolemic, hypervolemic, and euvolemic patients. This confirms that the selected features do not provide sufficient linear separability when reduced to two dimensions. The t-SNE

projections (Figures 5.12 and 5.14), while still lacking well-separated clusters, reveal more structured distributions. In the Linear SVM case, the samples are arranged along a curved manifold with partial class mixing. Notably, patients from different classes tend to align progressively along the same trajectory, suggesting that the model captures some form of monotonic organization, albeit not strictly class specific.

For the features selected by Random Forest, the t-SNE projection exhibits a similar distribution, though in the opposite direction. There is a spatial organization that may reflect non linear interactions among features, even though there is not a separation between classes. This observation is consistent with the model’s ability to exploit complex patterns rather than relying only on individual discriminative variables. In summary, these projections suggest that while the selected features do not lead to clear class separability in low dimensional space, both classifiers manage to extract useful structure.

6.2.3 Selection of a Minimal and Interpretable Feature Subset

Building upon the results of the statistical and machine learning analyses, a smaller and interpretable subset of features was identified. The statistical evaluation highlighted two clinical variables as particularly discriminative, in line with existing literature, and emphasized the relevance of diameter-related VIPER features. In contrast, the feature selection conducted through machine learning models confirmed *Edema* as the most consistently informative clinical variable, while among VIPER-derived parameters, collapsibility indices emerged as the most frequently selected across different feature combinations.

To identify a compact feature set that balances clinical interpretability and predictive performance, an exhaustive grid search was conducted using combinations of the most representative features from both domains—namely, the key clinical indicator for hypervolemia and selected VIPER metrics. The search was performed using both the Random Forest and Linear SVM classifiers.

The Random Forest model produced slightly better performance while requiring fewer features (Table 5.13), and was therefore chosen as the optimal model. Dimensionality reduction techniques (PCA and t-SNE) applied to this minimal subset revealed an improved organization of the data in the reduced space, as shown in Figures 5.15 and 5.16. Although fully distinct class clusters were still not observed, the new projections exhibited clearer groupings and a more structured distribution of samples, suggesting enhanced class-relevant separability with respect to the original feature sets.

These findings support the notion that a small number of carefully selected features can retain most of the discriminative information required for classification, particularly when the model is capable of detecting non-linear interactions. Moreover, the resulting feature set maintains clinical interpretability, potentially facilitating its use in practice for rapid assessment and decision-making in the context of

volemic status assessment in hyponatremic cases.

6.3 Repeatability of the measurements

This analysis was designed to evaluate the intra-operator repeatability and the variability of the automatic parameters, extracted using the VIPER software, across three acquisitions. The coefficient of variation (CoV) was computed over the three experimental sessions for each subject, providing a subject-specific estimate of repeatability. The CoV values were then averaged across all subjects to quantify the typical intra-operator variability expected for each parameter.

The results showed that the short-axis (SA) view provided more repeatable measurements than the long-axis (LA) view. As summarized in Table 5.2, all SA features exhibited lower CoV values compared to the corresponding LA features. This indicates reduced variability across repeated acquisitions by the same operator. These findings are consistent with the intraclass correlation coefficients, which confirmed excellent repeatability for most SA parameters, with ICC values exceeding 0.90 and narrow 95% confidence intervals. This indicates high consistency in repeated measurements on the same subject by the same operator.

In contrast, the lower ICC and higher CoV values observed for the LA view, especially for the caval index (CI: ICC = 0.62, CoV = 28.3%), reflect a greater intra-subject variability in these measurements.

This discrepancy may be explained by technical factors related to image acquisition and segmentation. Specifically, as presented in the previous chapter, some patients showed frames in which the IVC was not clearly visible due to partial disappearance in certain video segments (Figure 5.3), likely caused by bowel gas. In such cases, the segmentation algorithm may erroneously measure tissue outside the actual vessel, introducing random fluctuations across acquisitions. These outliers, resulting from poor image visibility or segmentation failure, can inflate intra-subject variability and therefore introduce bias in ICC computation, leading to underestimated repeatability.

All ICC values were statistically significant ($p < 0.001$) which confirmed that between subject variability was significantly greater than within subject variability, even though the F test results were lower for LA measurements. This indicates that the measurement is able to capture real physiological differences across patients and it is not just reflecting noise or measurement error.

6.4 Limits and Future Developments of the study

Despite the encouraging results, several limitations must be acknowledged. The most critical is the limited size of the population and the class imbalance of the patient. The hypovolemic class—clinically the most challenging to detect—was underrepresented, with only six cases, three of which lacked full short-axis acquisitions due to poor IVC visibility. This not only constrained the classifier’s ability to gen-

eralize to new patients in this group but may have also introduced a bias in the evaluation of feature importance. Furthermore, all data were acquired by a single operator, which prevented any assessment of inter-operator variability and limits the generalizability of the conclusions to other clinical settings. Although the VIPER software enabled semi-automatic tracking of IVC walls, the initial manual selection of the region of interest introduces a potential source of variability, particularly in the long-axis view, where lower repeatability was observed.

Looking ahead, future studies should aim to validate the findings on a larger and more balanced patient population, ideally across multiple centres, to ensure broader applicability. A particularly relevant direction would be to investigate whether comparable or superior classification performance can be achieved using only VIPER derived ultrasound features, eliminating the subjectivity introduced by clinical variables. In this regard, the use of deep learning approaches could be particularly valuable. In this study, the extracted signals were averaged across the duration of the video clips. Instead, another approach could be using the entire temporal sequences of diameter and collapsibility indices as input to time-series models such as recurrent neural networks or temporal convolutional networks. Such approaches could potentially capture patterns in the dynamic behaviour of the IVC that are lost through temporal aggregation.

In parallel, developing a fully automated pipeline that includes view detection, quality assessment and feature extraction without human intervention would increase clinical usability. Demonstrating a clear link between model predictions and patient prognosis would provide stronger evidence for the clinical utility of this approach and support its integration into decision making workflows.

In conclusion, this thesis provides preliminary but promising evidence that the combination of advanced ultrasound processing and machine learning can help in the accurate and reproducible classification of volume status in hyponatraemic patients. A fully automated version of this framework can be a more objective, accessible and time efficient volume status assessments in hyponatraemic patients directly at the bedside.

Chapter 7

Conclusion

The main problem in managing hyponatremia is the correct assessment of the patient's volume status, especially in the discrimination of the two most problematic groups, which are hypovolemic and euvoletic. Traditional volume status assessment are characterised by low specificity and sensitivity, so the aim of this study was to bring a more objective tool to help the classification. This study uses a semi-automatically tool, VIPER, which allow to process ultrasound videos in order to extract a set of parameters related to the inferior vena cava, with the aim to create a richer dataset that can help the classification. This thesis has shown that integrating VIPER derived ultrasound features with a minimal set of clinical variables can support the automated classification of volume status in hyponatraemic patients. In particular, the Random Forest classifier, trained on a reduced feature subset including *SA/CCI*, *LA/CCI*, *SA maximum diameter* and *Edema*, achieved promising results. It achieved, indeed, a balanced accuracy of 82% in leave-one-out cross-validation. These outcomes represent a step forward compared to traditional assessment strategies, based only on static ultrasound measurements or clinical judgement, which often lack reproducibility and objectivity.

The findings aligns with existing literature which highlight the limitations of IVC diameter alone as a discriminative feature, especially in euvoletic and hypovolemic states. Moreover, they support the idea of using also dynamic indices such as the collapsibility indeces. This work benefits from the availability of both long- and short-axis ultrasound acquisitions, while previous studies often focus on single view measurements or limited indices. Moreover, the high intra-operator repeatability of short-axis measurements reinforces the reliability of these features in a clinical context, especially for diameter and collapsibility indices (ICCs > 0.90).

Bibliography

- [1] Pierpaolo Di Nicolò et al. “Inferior Vena Cava ultrasonography for volume status evaluation: An intriguing promise never fulfilled”. en. In: *Journal of clinical medicine* 12.6 (2023). ISSN: 2077-0383. DOI: 10.3390/jcm12062217. URL: <http://dx.doi.org/10.3390/jcm12062217>.
- [2] Vi Dinh. *VExUS ultrasound Score – Fluid Overload and Venous Congestion assessment*. en. URL: <https://www.pocus101.com/vexus-ultrasound-score-fluid-overload-and-venous-congestion-assessment/>.
- [3] Can Ekinici et al. “Effects of volume overload and current techniques for the assessment of fluid status in patients with renal disease”. en. In: *Blood purification* 46.1 (2018), pp. 34–47. ISSN: 0253-5068. DOI: 10.1159/000487702. URL: <http://dx.doi.org/10.1159/000487702>.
- [4] Connor Evins and Aniel Rao. “Point-of-care ultrasound to evaluate volume status in severe hyponatremia”. en. In: *BMJ case reports* 13.6 (2020), e235304. ISSN: 1757-790X. DOI: 10.1136/bcr-2020-235304. URL: <http://dx.doi.org/10.1136/bcr-2020-235304>.
- [5] Anna Folino et al. “Vena Cava responsiveness to controlled isovolumetric respiratory efforts”. en. In: *Journal of ultrasound in medicine: official journal of the American Institute of Ultrasound in Medicine* 36.10 (2017), pp. 2113–2123. ISSN: 0278-4297. DOI: 10.1002/jum.14235. URL: <http://dx.doi.org/10.1002/jum.14235>.
- [6] *Gradient boosting, random forests, bagging, voting, stacking*. en. URL: <https://scikit-learn.org/stable/modules/ensemble.html>.
- [7] John E. Hall. *Guyton and hall textbook of medical physiology*. en. 13th ed. London, England: W B Saunders, 2015. ISBN: 9781455770052.
- [8] Seyed Mehrdad Hamrahian. *Hyponatremia*. en. Jan. 2025. URL: https://emedicine.medscape.com/article/242166-overview?utm_source=chatgpt.com.
- [9] Ewout J. Hoorn and Robert Zietse. “Diagnosis and treatment of hyponatremia: Compilation of the guidelines”. en. In: *Journal of the American Society of Nephrology: JASN* 28.5 (2017), pp. 1340–1349. ISSN: 1046-6673. DOI: 10.1681/ASN.2016101139. URL: <http://dx.doi.org/10.1681/ASN.2016101139>.

- [10] Richard J. Johnson et al. *Comprehensive Clinical Nephrology*. 6th ed. Elsevier, 2018. ISBN: 9780323547192.
- [11] G. Joseph. “Treatment of Hyponatremia: Expert Panel Recommendations Verbalis”. In: *The American Journal of Medicine* 126.10 (2013), S1–S42.
- [12] Matthew J. Kaptein and Elaine M. Kaptein. “Inferior Vena Cava collapsibility index: Clinical validation and application for assessment of relative intravascular volume”. en. In: *Advances in chronic kidney disease* 28.3 (2021), pp. 218–226. ISSN: 1548-5595. DOI: 10.1053/j.ackd.2021.02.003. URL: <http://dx.doi.org/10.1053/j.ackd.2021.02.003>.
- [13] Jae Seok Kim et al. “Estimation of body fluid volume by bioimpedance spectroscopy in patients with hyponatremia”. en. In: *Yonsei medical journal* 55.2 (2014), pp. 482–486. ISSN: 0513-5796. DOI: 10.3349/ymj.2014.55.2.482. URL: <http://dx.doi.org/10.3349/ymj.2014.55.2.482>.
- [14] Abhilash Koratala and Amir Kazory. “Point of care ultrasonography for objective assessment of heart failure: Integration of cardiac, vascular, and extravascular determinants of volume status”. en. In: *Cardiorenal medicine* 11.1 (2021), pp. 5–17. ISSN: 1664-3828. DOI: 10.1159/000510732. URL: <http://dx.doi.org/10.1159/000510732>.
- [15] Sennur Budak Kose et al. “Bioimpedance spectroscopy for the differential diagnosis of hyponatremia”. en. In: *Renal failure* 37.6 (2015), pp. 947–950. ISSN: 0886-022X. DOI: 10.3109/0886022X.2015.1040418. URL: <http://dx.doi.org/10.3109/0886022X.2015.1040418>.
- [16] Gilles Louppe. “Understanding random forests: From theory to practice”. In: (2014). DOI: 10.13140/2.1.1570.5928. URL: <http://dx.doi.org/10.13140/2.1.1570.5928>.
- [17] Jaime Mazón Ruiz et al. “Medicina de precisión: «Point of Care Ultrasound» (PoCUS) en el abordaje diagnóstico del paciente con hiponatremia”. es. In: *Nefrología: publicación oficial de la Sociedad Española Nefrología* 44.2 (2024), pp. 159–164. ISSN: 0211-6995. DOI: 10.1016/j.nefro.2023.02.011. URL: <http://dx.doi.org/10.1016/j.nefro.2023.02.011>.
- [18] Luca Mesin, Paolo Pasquero, and Silvestro Roatta. “Multi-directional assessment of respiratory and cardiac pulsatility of the inferior Vena Cava from ultrasound imaging in short axis”. en. In: *Ultrasound in medicine & biology* 46.12 (2020), pp. 3475–3482. ISSN: 0301-5629. DOI: 10.1016/j.ultrasmedbio.2020.08.027. URL: <http://dx.doi.org/10.1016/j.ultrasmedbio.2020.08.027>.
- [19] Luca Mesin, Paolo Pasquero, and Silvestro Roatta. “Tracking and monitoring pulsatility of a portion of inferior Vena Cava from ultrasound imaging in long axis”. en. In: *Ultrasound in medicine & biology* 45.5 (2019), pp. 1338–1343. ISSN: 0301-5629. DOI: 10.1016/j.ultrasmedbio.2018.10.024. URL: <http://dx.doi.org/10.1016/j.ultrasmedbio.2018.10.024>.

- [20] Luca Mesin et al. “Assessment of phasic changes of vascular size by automated edge tracking-state of the art and clinical perspectives”. en. In: *Frontiers in cardiovascular medicine* 8 (2021), p. 775635. ISSN: 2297-055X. DOI: 10.3389/fcvm.2021.775635. URL: <http://dx.doi.org/10.3389/fcvm.2021.775635>.
- [21] Luca Mesin et al. “Improved repeatability of the estimation of pulsatility of inferior Vena Cava”. en. In: *Ultrasound in medicine & biology* 45.10 (2019), pp. 2830–2843. ISSN: 0301-5629. DOI: 10.1016/j.ultrasmedbio.2019.06.002. URL: <http://dx.doi.org/10.1016/j.ultrasmedbio.2019.06.002>.
- [22] Luca Mesin et al. “Semi-automated tracking and continuous monitoring of inferior vena cava diameter in simulated and experimental ultrasound imaging”. en. In: *Ultrasound in medicine and biology* 41.3 (2015), pp. 845–857. ISSN: 0301-5629. DOI: 10.1016/j.ultrasmedbio.2014.09.031. URL: <http://dx.doi.org/10.1016/j.ultrasmedbio.2014.09.031>.
- [23] Alessandro Peri. “Management of hyponatremia: causes, clinical aspects, differential diagnosis and treatment”. en. In: *Expert review of endocrinology & metabolism* 14.1 (2019), pp. 13–21. ISSN: 1744-6651. DOI: 10.1080/17446651.2019.1556095. URL: <http://dx.doi.org/10.1080/17446651.2019.1556095>.
- [24] Jakub Piotrkowski et al. “Use of bedside ultrasound to assess fluid status: a literature review”. en. In: *Polish archives of internal medicine* 129.10 (2019), pp. 692–699. DOI: 10.20452/pamw.14962. URL: <http://dx.doi.org/10.20452/pamw.14962>.
- [25] Latif R. Rahman et al. “Point-of-care ultrasound is a useful adjunct tool to a clinician’s assessment in the evaluation of severe hyponatraemia”. en. In: *Clinical endocrinology* 100.6 (2024), pp. 595–601. ISSN: 0300-0664. DOI: 10.1111/cen.15024. URL: <http://dx.doi.org/10.1111/cen.15024>.
- [26] Helbert Rondon and Madhu Badireddy. “Hyponatremia”. en. In: *StatPearls*. Treasure Island (FL): StatPearls Publishing, 2025.
- [27] Lawrence G. Rudski et al. “Guidelines for the echocardiographic assessment of the right heart in adults: a report from the American Society of Echocardiography endorsed by the European Association of Echocardiography, a registered branch of the European Society of Cardiology, and the Canadian Society of Echocardiography”. en. In: *Journal of the American Society of Echocardiography: official publication of the American Society of Echocardiography* 23.7 (2010), 685–713, quiz 786–8. ISSN: 0894-7317. DOI: 10.1016/j.echo.2010.05.010. URL: <http://dx.doi.org/10.1016/j.echo.2010.05.010>.
- [28] Samira Samant and Abhilash Koratala. “Point-of-care Doppler ultrasound in the management of hyponatremia: Another string to nephrologists’ Bow”. en. In: *Clinical case reports* 9.8 (2021), e04687. ISSN: 2050-0904. DOI: 10.1002/ccr3.4687. URL: <http://dx.doi.org/10.1002/ccr3.4687>.

- [29] Mahmud Saqib, Gregory Capelli, and Abhilash Koratala. “Utility of nephrologist-performed point of care ultrasonography in the evaluation of hyponatremia”. en. In: *POCUS journal* 7.Kidney (2022), pp. 11–13. ISSN: 2369-8543. DOI: 10.24908/pocus.v7iKidney.15339. URL: <http://dx.doi.org/10.24908/pocus.v7iKidney.15339>.
- [30] E. Sbardella et al. “Approach to hyponatremia according to the clinical setting: Consensus statement from the Italian Society of Endocrinology (SIE), Italian Society of Nephrology (SIN), and Italian Association of Medical Oncology (AIOM)”. en. In: *Journal of endocrinological investigation* 41.1 (2018), pp. 3–19. ISSN: 0391-4097. DOI: 10.1007/s40618-017-0776-x. URL: <http://dx.doi.org/10.1007/s40618-017-0776-x>.
- [31] Parth Shah and Martine A. Louis. “Physiology, central venous pressure”. en. In: *StatPearls*. Treasure Island (FL): StatPearls Publishing, 2025.
- [32] Ragav Sharma and Sandeep Sharma. “Physiology, blood volume”. en. In: *StatPearls*. Treasure Island (FL): StatPearls Publishing, 2025.
- [33] İlker Şirin, Gülşen Çığşar, and Bedriye Müge Sönmez. “The role of ultrasonographic inferior Vena Cava measurement in the volume-based classification of patients with hyponatremia”. en. In: *Journal of ultrasound in medicine: official journal of the American Institute of Ultrasound in Medicine* 42.10 (2023), pp. 2391–2401. ISSN: 0278-4297. DOI: 10.1002/jum.16266. URL: <http://dx.doi.org/10.1002/jum.16266>.
- [34] Tomohiro Sonoo et al. “Prospective analysis of cardiac collapsibility of inferior vena cava using ultrasonography”. en. In: *Journal of critical care* 30.5 (2015), pp. 945–948. ISSN: 0883-9441. DOI: 10.1016/j.jcrc.2015.04.124. URL: <http://dx.doi.org/10.1016/j.jcrc.2015.04.124>.
- [35] Goce Spasovski et al. “Clinical practice guideline on diagnosis and treatment of hyponatraemia”. en. In: *European journal of endocrinology* 170.3 (2014), G1–47. ISSN: 0804-4643. DOI: 10.1530/EJE-13-1020. URL: <http://dx.doi.org/10.1530/EJE-13-1020>.
- [36] Georgios Spentzouris et al. “The clinical anatomy of the inferior vena cava: a review of common congenital anomalies and considerations for clinicians: Inferior Vena Cava”. en. In: *Clinical anatomy (New York, N.Y.)* 27.8 (2014), pp. 1234–1243. ISSN: 0897-3806. DOI: 10.1002/ca.22445. URL: <http://dx.doi.org/10.1002/ca.22445>.
- [37] Cindy L. Stanfield. *Principles of human physiology*. 6th ed. Upper Saddle River, NJ: Pearson, 2016. ISBN: 9780134169804.
- [38] *Support vector machines*. en. URL: <https://scikit-learn.org/stable/modules/svm.html>.
- [39] William D. Tucker, Ribesh Shrestha, and Bracken Burns. “Anatomy, abdomen and pelvis: Inferior Vena Cava”. en. In: *StatPearls*. Treasure Island (FL): StatPearls Publishing, 2025.

- [40] Rita Varudo et al. “Use of Venous Excess UltraSound (VExUS) score in hyponatraemia management in critically ill patient”. en. In: *BMJ case reports* 15.2 (2022), e246995. ISSN: 1757-790X. DOI: 10.1136/bcr-2021-246995. URL: <http://dx.doi.org/10.1136/bcr-2021-246995>.
- [41] Vineet Veitla and Bhavna Bhasin. “Focused cardiac assessment in kidney care”. en. In: *POCUS journal* 7.Kidney (2022), pp. 45–50. ISSN: 2369-8543. DOI: 10.24908/pocus.v7iKidney.14996. URL: <http://dx.doi.org/10.24908/pocus.v7iKidney.14996>.